

# Collapse of Eurasian ice sheets 14,600 years ago was a major source of global Meltwater Pulse 1a

*Preprint submitted to Eartharxiv August 20th, 2019*

Jo Brendryen<sup>1,2,3,\*</sup>, Hafidi Hafidason<sup>1,2</sup>, Yusuke Yokoyama<sup>4</sup>,  
Kristian Agasøster Haaga<sup>1,2,3</sup>, and Bjarte Hannisdal<sup>1,2,3</sup>

<sup>1</sup>Department of Earth Science, University of Bergen, Norway

<sup>2</sup>Bjerknes Centre for Climate Research, University of Bergen

<sup>3</sup>K.G. Jebsen Centre for Deep Sea Research, University of Bergen

<sup>4</sup>Atmosphere and Ocean Research Institute, University of Tokyo, Japan

\*Corresponding author: [jo.brendryen@uib.no](mailto:jo.brendryen@uib.no)

**Rapid sea-level rise caused by the collapse of large ice sheets is a global threat to human societies<sup>1</sup>. In the last deglacial period, the rate of global sea-level rise peaked at more than 4 cm/yr during Meltwater Pulse 1a, which coincided with the abrupt Bølling warming event ~14,650 yr ago<sup>2-5</sup>. However, the sources of the meltwater have proven elusive<sup>6,7</sup>, and the contribution from Eurasian ice sheets has until now been considered negligible<sup>8-10</sup>. Here we show that marine-based sectors of the Eurasian ice sheet complex collapsed at the Bølling transition and lost an ice volume of between 4.5 and 7.9 m sea level equivalents (95% quantiles) over 500 yr. During peak melting 14,650 - 14,310 yr ago, Eurasian ice sheets lost between 3.3 and 6.7 m sea level equivalents (95% quantiles), thus contributing significantly to Meltwater Pulse 1a. A mean meltwater flux of 0.2 Sv over 300 yr was injected into the Norwegian Sea and the Arctic Ocean during a time when proxy evidence suggests vigorous Atlantic meridional overturning circulation<sup>11,12</sup>. Our reconstruction of the EIS deglaciation shows that a marine-based ice sheet comparable in size to the West Antarctic ice sheet can collapse in as little as 300-500 years.**

Understanding the response of marine-based ice sheets to global warming is critical to future sea-level projections<sup>1</sup>. Today large marine-based ice sheets are situated in the Antarctic, with the West Antarctic ice sheet long considered to be particularly vulnerable<sup>13-16</sup>. The time scale and magnitude of its potential disintegration are highly uncertain, however, and its projected contribution to sea-level rise over the next centuries varies by orders of magnitude<sup>17,18</sup>. To add further empirical constraints, researchers turn to past deglaciation events to study the tempo and mode of ice sheet collapse in a warming world. The West Antarctic ice sheet itself survived the end of the last ice age, but an important analogue can be found in the collapse of the Late Pleistocene Eurasian ice sheet complex (EIS) (Fig. 1).

During the last glacial maximum, 20-21 kyr ago, the EIS attained a maximum ice volume of ~24 m global sea level equivalents (SLE)<sup>19</sup>, including large marine-based sectors extending all the way to the continental shelf edge. These sectors formed an extensive interface to the Arctic Ocean and the Nordic Seas, which are one of the main loci of deep-water formation essential to the Atlantic Meridional Overturning Circulation (AMOC). This region is thus of particular importance for understanding the impact of meltwater forcing on ocean circulation and global climate<sup>20</sup>.

At the end of the last ice age, abrupt Northern Hemisphere warming at the Bølling transition ~14,650 yr BP coincided with accelerated melting of ice sheets in an event known as global Meltwater Pulse 1a (MWP-1a)<sup>2-5</sup>. During this event, mean global sea-level rose by 12-14 m in ~340 yr, at a rate of at least 4 cm/yr<sup>5</sup>. The sources, magnitude and timing of the MWP-1a have been a subject of controversy over the past decades, and a significant role for the EIS has until now been largely dismissed<sup>6,8,10</sup>. Previous reconstructions of the EIS deglaciation and meltwater contributions<sup>8,19,21</sup> have concluded that the bulk of the marine sectors were deglaciated well before the Bølling transition and the MWP-1a. These reconstructions have, however, assumed a constant marine radiocarbon reservoir age ( $R$ ) similar to the modern value throughout the deglaciation, typically around 400 yr. Although the uncertainty of this assumption is commonly acknowledged, a lack of constraints on the temporal evolution of  $R$  in the Norwegian Sea has prevented a more accurate reconstruction of the deglaciation.

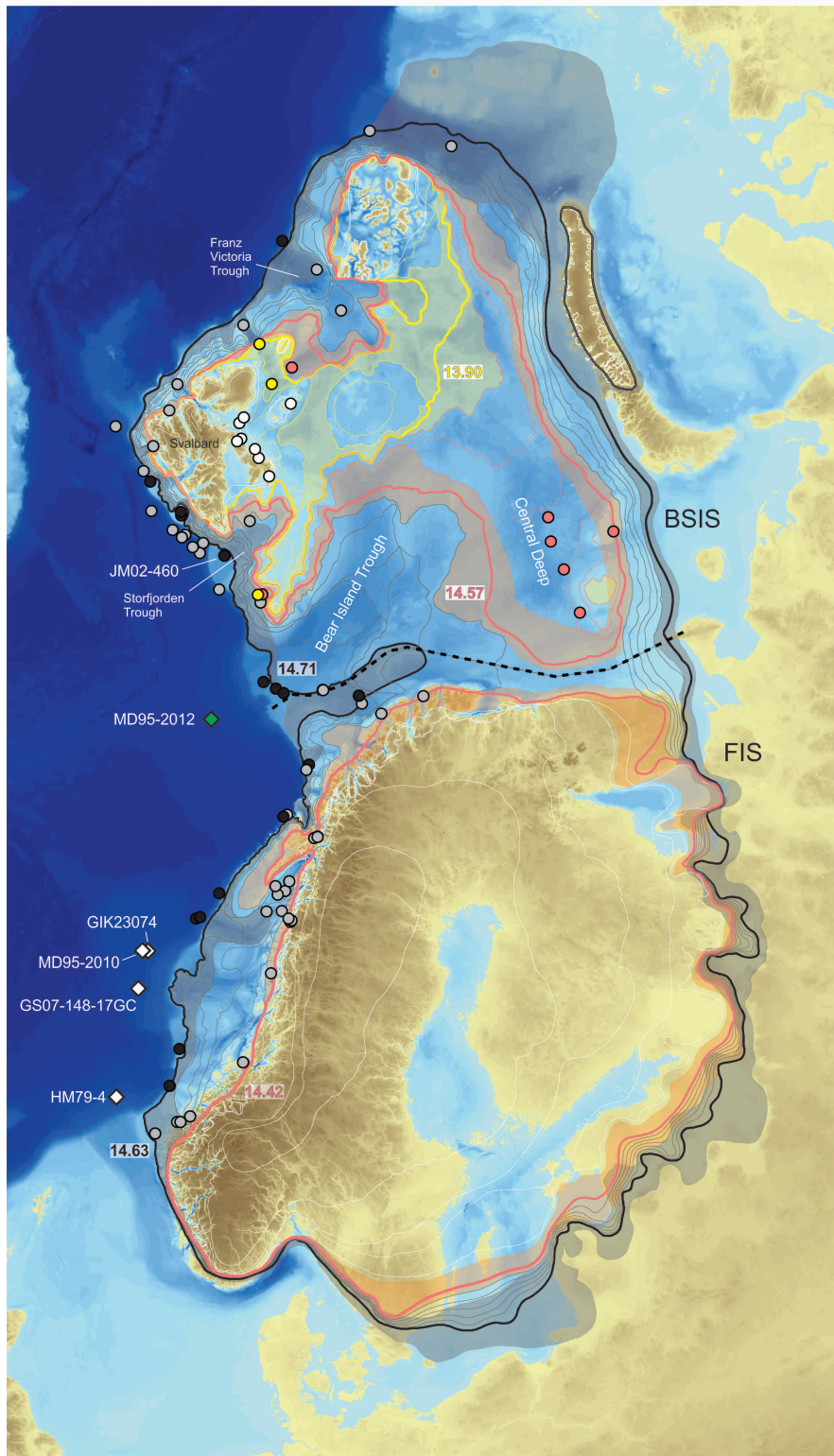


Figure 1: Reconstructed Late Pleistocene EIS complex comprised of the Fennoscandian Ice Sheet (FIS) and the Barents-Svalbard Ice Sheet (BSIS). Contour lines represent ice margins at different stages of the deglaciation. Thick lines represent ice margin positions at boundaries between the deglacial phases used in the Bayesian chronology (Supplementary Data Fig. 7 and 8 and Supplementary Data File). Black lines are the inferred ice margin following the late Heinrich Stadial 1 ice advance. Pink lines are the ice margins that followed the separation of the BSIS and FIS. Yellow lines mark ice margins when the BSIS are constrained on the archipelagos and shallow banks in the northern Barents sea. The median age of each margin is indicated. The accompanying transparent fields mark the geographic uncertainties associated with the respective ice margins. Thin lines mark the suggested ice sheet retreat pattern within each phase as synthesized from the literature listed in [Methods](#). The black stippled line marks the separation between the FIS and the BSIS used in the area-volume calculation when they were confluent. Black filled circles mark sites used to constrain the Heinrich Stadial 1 extent of the ice sheet. The positions of the stratigraphic records and dates used to constrain the deglacial phases are marked with gray, pink, yellow and white filled circles. White diamonds mark the position of cores used to reconstruct the Norwegian Sea  $^{14}\text{C}$  reservoir age. White lines indicate ice margins adopted from the Dated-1 reconstruction.

## 49 Norwegian Sea $^{14}\text{C}$ reconstruction and deglacial chronology

50 We here present a new chronology for the deglaciation of the marine-based sectors of the EIS complex,  
51 using new constraints on the Norwegian Sea  $^{14}\text{C}$  and  $R$  to calibrate marine  $^{14}\text{C}$  dates linked to the retreat  
52 of the EIS. We take advantage of the close connection between North Atlantic climate and the Asian Mon-  
53 soon<sup>22-26</sup> to align Norwegian Sea paleoceanographic records with a U/Th-dated speleothem record from  
54 Hulu Cave, China<sup>27,28</sup> (Fig. 2; Methods; Supplementary Fig. 1). This alignment is corroborated by a  
55 tephrochronological marker bed found both in Norwegian Sea sediments and Greenland ice cores (Supple-  
56 mentary Fig. 1, Methods). The age difference between 99  $^{14}\text{C}$  dates compiled from these same cores and  
57 the corresponding atmospheric  $^{14}\text{C}$  age represented by the IntCal13 calibration curve<sup>29</sup> (Fig. 2F) yields a  
58 new and detailed account of the temporal evolution of the Norwegian Sea  $^{14}\text{C}$  reservoir age from 19,000 to  
59 12,500 yr BP (Fig. 2G).

60 Prior to the Bølling warming, the Norwegian Sea had a mean  $R$  of 1,620  $^{14}\text{C}$  yr (Fig. 2G). Then, at the  
61 Bølling transition,  $R$  abruptly declined by  $\sim 1,500$   $^{14}\text{C}$  yr in less than 400 calendar yr and the mean  $R$  for the  
62 remainder of the warm period was 420  $^{14}\text{C}$  yr (Fig. 2). We resample (Methods) the compiled timeseries of  
63  $^{14}\text{C}$  ages by a Monte Carlo technique where chronological, stratigraphical and  $^{14}\text{C}$  uncertainties are taken  
64 into account (Fig. 2F) and use this to calibrate published conventional radiocarbon ages from sedimentary  
65 archives that are linked to the dynamics and deglaciation of marine-based sectors of the EIS. The deglacia-  
66 tion of the EIS complex is reconstructed using a probabilistic approach, taking into account uncertainty in  
67 both area and age (Methods). The resulting estimates are reported here as medians and 95% quantiles from  
68 the probability distributions. The deglaciation for the BSIS and FIS is constrained independently, yielding  
69 a sequence of reconstructed ice margins with uncertainty bounds (Fig. 1).

70 Our revised EIS chronology (Supplementary Figs. 7 and 8; Supplementary Data File) suggests that  
71 the Barents-Svalbard ice sheet (BSIS) remained in an advanced position until 14.71 (14.81-14.63) kyr cal  
72 BP, after which it rapidly retreated from the outer shelf and deeper troughs at the Bølling transition. At  
73 14.57 (14.67-14.46) kyr cal BP, the BSIS had separated from the Fennoscandian ice sheet, forming an  
74 ice lobe over the Central Deep in the Barents Sea, and by 13.90 (14.20-13.57) kyr cal BP it had become  
75 confined to islands and shallow banks in the northern Barents Sea (Fig. 1). The reconstructed retreat of the  
76 BSIS is congruent with a prominent early Bølling meltwater  $\delta^{18}\text{O}$  anomaly observed in proxy records from  
77 core MD95-2012 retrieved from the Barents Sea margin<sup>35,36</sup>. Deglaciation of the Fennoscandian ice sheet  
78 commenced at 14.63 (14.78-14.49) kyr cal BP, and by 14.42 (14.57-14.20) kyr cal BP it had retreated from  
79 the continental shelf into the coastal areas (Fig. 1).

## 80 EIS collapse and MWP-1a contribution

81 Based on the area-volume relationship for extant ice sheets<sup>37</sup>, our reconstruction implies that before the  
82 Bølling transition, the EIS contained an ice volume of 15.0 (13.9-16.1) m SLE (Figure 2H). We also applied  
83 an alternative area-volume regression using the output of a transient model of the EIS complex itself<sup>38</sup>  
84 (Supplementary Fig. 9). Although the alternative regression yields an EIS volume that is 2.7 m SLE less  
85 than the Paterson approximation at the start of the deglaciation, the estimated ice loss between 14.7 and  
86 14.4 kyr BP differs by only  $\sim 0.2$  m SLE, which is negligible with respect to our conclusions. Hence, our  
87 mass loss estimates are robust to the assumptions of the area-volume conversion (Supplementary Fig. 9).

88 Our new reconstruction implies that the marine-based EIS collapsed at the Bølling transition. Over  
89 a 500 yr period, starting at 14.71 cal kyr BP, the EIS lost a volume of 6.2 (4.5-7.9) m SLE. Within the  
90 MWP-1a time span as defined by the Tahiti chronology (14.65-14.31 kyr BP)<sup>5</sup>, the EIS lost a volume of  
91 4.9 (3.3-6.7) m SLE, implying that the collapse of the EIS was a major source of the MWP-1a. Given the  
92 presence of ichnofabric in parts of the Norwegian Sea core sediments, we show that bioturbation would  
93 result in the smearing out of a more abrupt change in the reservoir age occurring close to the Bølling  
94 transition, effectively shifting the start of the  $R$  decline back in time by more than 200 calendar years  
95 (Methods; Supplementary Fig. 6). Therefore, our mass loss estimates are likely to be conservative, in the  
96 sense that they may overestimate the time span of the EIS collapse and thus underestimate its contribution  
97 to the MWP-1a.

## 98 Implications for deglaciation and ice sheet collapse

99 An EIS contribution of 4.9 (3.3-6.7) m SLE to the MWP-1a is substantially larger than previous estimates  
100 in Dated-1<sup>19</sup> (1.1 m SLE when interpolated to 340 yr from the most-credible Dated-1 ice margins at 15

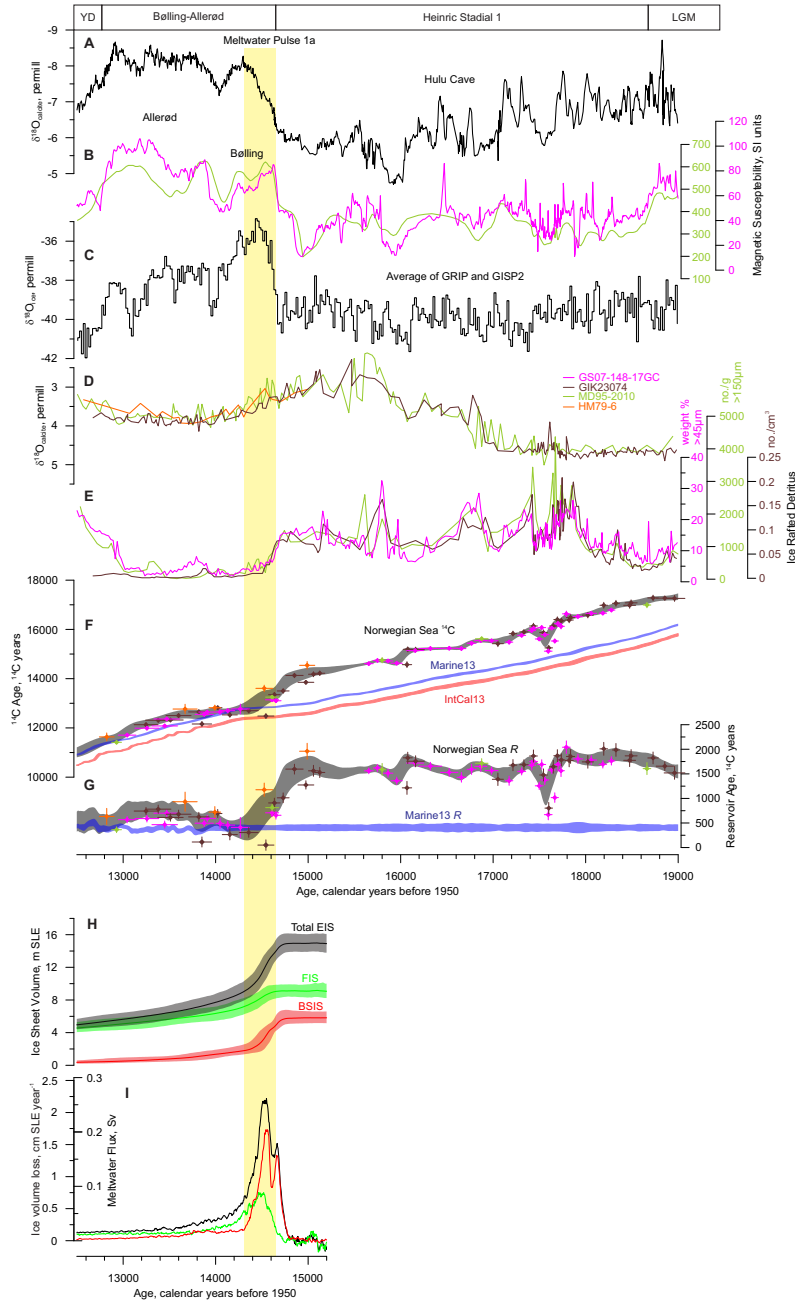


Figure 2: Records of climate, ice volume and meltwater flux from the Eurasian Ice Sheet complex. **A**,  $\delta^{18}\text{O}$  record from Hulu cave speleothem H82. **B**, Magnetic susceptibility from two Norwegian sea sediment cores (Fig. 1), aligned with the speleothem  $\delta^{18}\text{O}$  record in **(A)**. **C**, Average  $\delta^{18}\text{O}$  record from Greenland summit ice cores (GISP2 and GRIP) on the GICC05 chronology. **D**, Planktonic foraminifera  $\delta^{18}\text{O}$  (*Neoglobigerina pachyderma* sinistral) from three Norwegian Sea sediment cores. **E**, Proxy records of ice rafted detritus from Norwegian Sea cores. **F**, Compiled AMS  $^{14}\text{C}$  ages from Norwegian Sea sediment cores (GS07-148-17GC, this study; GIK23074; MD95-2010; HM79-6). Horizontal error bars represent the 68.2% quantiles (equivalent to  $1\sigma$ ) of the GS07-148-17GC deposition model. Gray shading represents  $\pm 1\sigma$  of the Monte Carlo sampling of the probability density functions of both the stratigraphic and chronological core alignments and the  $^{14}\text{C}$  uncertainty. **G**, Norwegian Sea  $^{14}\text{C}$  reservoir age,  $R$  is calculated as the difference between the conventional  $^{14}\text{C}$  ages (at the median age) and the IntCal13 atmospheric  $^{14}\text{C}$  curve. Vertical error bars are the root sum of squares of the  $^{14}\text{C}$  uncertainties. The average global reservoir age represented by the Marine13 calibration curve is plotted for reference. **H**, Reconstructed ice volume for the Eurasian Ice Sheet (EIS) complex expressed as sea level equivalents (SLE; 25 yr running mean of median and 95% quantiles). FIS: Fennoscandian Ice Sheet; BSIS: Barents-Svalbard Ice Sheet. **I**, median rate of ice volume loss in cm SLE per yr and as meltwater flux (Sv) (colors as in **(H)**).

101 and 14 kyr BP), and is comparable to the estimated contribution from the much larger North American ice  
 102 sheet (5-6 m SLE in ref. <sup>39</sup>, 6.4-9 m SLE (interpolated to 340 yr) in ref. <sup>40</sup>, and 4-7 m SLE in ref. <sup>10</sup>).  
 103 Although a prominent MWP-1a contribution from the EIS is consistent with observed sea-level fingerprints <sup>9</sup>,  
 104 the inferred total amplitude of the MWP-1a and the distribution of other meltwater sources need to be  
 105 reconsidered in light of our findings <sup>5,6</sup>.

106 Observed records of relative sea-level fall in Scotland do not support the predicted sea-level finger-  
 107 prints from a glacio-isostatic model of the MWP-1a when sourced solely from the Laurentide ice sheet and  
 108 Antarctica, but this discrepancy may be reconciled by a larger meltwater contribution from the EIS <sup>41</sup>. A  
 109 large EIS contribution is also consistent with near-field records from both western and northern Norway  
 110 that show falling relative sea-level during the Bølling <sup>42-44</sup>, as expected if gravitational and isostatic effects  
 111 from EIS mass loss overwhelmed eustatic sea-level rise from the MWP-1a.

112 Modeled far-field sea-level fingerprints suggest that a MWP-1a sourced from the EIS would increase  
 113 the local sea-level by about 10 % at Tahiti and by 4 % at the Sunda shelf <sup>9</sup>. This proportional increase would  
 114 translate our conservative estimates of EIS mass loss during the MWP-1a into 3.6-7.4 m relative sea level  
 115 rise at Tahiti and 3.3-7.0 m at the Sunda shelf. If we consider the observed low-end local sea-level rise of 12  
 116 m at Tahiti <sup>5</sup>, then our results suggest that the EIS collapse may have contributed 30-60 % of the MWP-1a

117 at this locality. For the high-end local sea level rise estimate of 17.3 m at the Sunda shelf<sup>6</sup>, our mass loss  
118 estimates correspond to 20-40% of the local sea level rise. A more accurate estimate of the eustatic sea-  
119 level contribution from the EIS collapse will require additional constraints on the effect of glacio-isostasy  
120 and ice volume below flotation. Nevertheless, our findings provide strong empirical evidence that the EIS  
121 was a major source of the MWP-1a. Combined with recent estimates for the North American Ice Sheet  
122 MWP-1a contribution<sup>10,40</sup> our EIS mass loss estimates are sufficient for explaining the far-field relative sea  
123 level observations without a major Antarctic contribution, consistent with the lack of field evidence for a  
124 large retreat of the Antarctic Ice Sheet<sup>45</sup>.

125 Our new account of the EIS collapse is an important step towards solving the mysteries of the Bølling  
126 event and the MWP-1a, which also raises a number of research questions pertinent to climate change sce-  
127 narios for the near future.

128 (1) What triggered the collapse of the marine-based EIS? In addition to the abrupt atmospheric and  
129 surface ocean warming at the Bølling transition<sup>32,46,47</sup>, proxy records from core JM02-460 suggest a marked  
130 subsurface warming on the Barents Sea continental shelf during the late Heinrich Stadial 1<sup>48</sup>, close to the  
131 inferred ice sheet grounding line (Fig. 1). A vast ice-ocean interface rendered marine-based EIS sectors  
132 potentially very sensitive to subsurface warming and melting at the grounding line, which is considered to  
133 be one of the main drivers of current<sup>49,50</sup> and past<sup>51</sup> mass loss from the Antarctic ice sheets.

134 (2) Which mechanisms drove the rapid EIS retreat? In addition to surface melting and the likely in-  
135 volvement of mass-balance/elevation feedback<sup>39</sup>, continuity between subglacially carved lineations and  
136 iceberg ploughmarks in the Bear Island Trough suggests calving of deep-keeled icebergs at the ice front<sup>52</sup>.  
137 These findings are consistent with the operation of the marine ice cliff instability mechanism (MICI)<sup>53,54</sup>  
138 during the rapid ice sheet retreat. The current water depth in the SW Barents Sea is 400-500 m, less than  
139 the ~800 m thought to be required by MICI<sup>53</sup>. Isostatic depression by ice sheet loading<sup>55</sup>, however, may  
140 have lowered the bed sufficiently for this mechanism to operate. Alternatively, the MICI may operate at  
141 shallower depths than currently parameterized in models. Although past Antarctic deglaciation events can  
142 be explained without invoking this specific mechanism<sup>56</sup>, the MICI is featured in the model yielding the  
143 high-end future rate of ice loss from the Antarctic Ice Sheet<sup>18</sup>.

144 (3) What was the impact of EIS meltwater on ocean circulation? We estimate that a meltwater flux of  
145 0.2 Sv over 300 yr was injected into the Norwegian Sea and the Arctic Ocean during the early Bølling, a  
146 time period when proxy evidence suggests vigorous Atlantic meridional overturning circulation<sup>11,12,57</sup>. This  
147 result implies that the relationship between freshwater injection and North Atlantic deep water formation is  
148 not clear-cut, and highlights the need to resolve meltwater routing<sup>58</sup>.

149 Our reconstruction of the EIS deglaciation shows that an ice sheet comparable in size to the West  
150 Antarctic ice sheet can collapse in as little as 300-500 years. Ice sheet models used to predict the future of  
151 marine-based Antarctic ice sheets differ markedly in their predicted rates of ice loss and in the mechanisms  
152 involved<sup>17,18</sup>. We provide new empirical constraints that raise the prospect of using the marine-based EIS  
153 collapse as a benchmark for validating such ice sheet models and ultimately improve projections of future  
154 sea-level rise. The estimated rates of ice loss from the EIS during the early Bølling (~1.6 cm SLE yr<sup>-1</sup>  
155 averaged over 300 yr, peaking at ~2.2 cm SLE yr<sup>-1</sup>) are comparable to high-end values of mass loss  
156 projected for the West Antarctic ice sheet in the next centuries.

## 157 **Methods**

### 158 **Temporal evolution of the marine radiocarbon reservoir age (*R*)**

159 We compiled a time series of 41 new and 58 previously published AMS <sup>14</sup>C ages of the polar subsurface-  
160 dwelling planktonic foraminifer *Neoglobigerina pachyderma* sinistral, from four Norwegian Sea sediment  
161 cores (Fig. 2).

162 Sediments from core GS07-148-17GC were continuously sampled in 0.5 cm thick slices that were dried  
163 and washed over 45 and 100 μm sieves. From the >100 μm grain size fraction, 47 samples of monospecific  
164 *Neoglobigerina pachyderma* (sinistral) were picked and measured for <sup>14</sup>C at the Atmosphere and Ocean  
165 Research Institute (AORI) at the University of Tokyo. Foraminiferal tests were weighed and washed ultra-  
166 sonically before converting them into graphite under the protocol described in<sup>59</sup>. For samples smaller than  
167 0.3 mgC, a specially designed high vacuum line was used for the preparation<sup>60</sup>. Target graphite was then  
168 measured by the single stage accelerator mass spectrometer at AORI<sup>61</sup>.

169 The <sup>14</sup>C data and other records from three of the cores (MD95-2010, HM79-6 and GIK23074) are  
170 previously published<sup>31-34</sup>. These cores were stratigraphically aligned to core GS07-148-17GC using tie-  
171 points defined by a combination of records of ice rafted detritus (IRD), magnetic susceptibility (MS) and the

172  $\delta^{18}\text{O}$  and  $\delta^{13}\text{C}$  of *N. pachyderma* sinistral (Supplementary Fig. 4). The alignment to the GS07-148-17GC  
173 depth scale was performed with the Oxcal v4.3.2 software<sup>62</sup>, using the P\_Sequence sediment deposition  
174 model<sup>63</sup> and the variable  $k$  option<sup>64</sup>. We assume an uncertainty of  $\pm 2$  cm ( $1\sigma$ ) for each tie-point.

175 Absolute age control of the core records including  $^{14}\text{C}$  was obtained by event-stratigraphic correlation  
176 with the U/Th dated H82 speleothem  $\delta^{18}\text{O}$  record from Hulu Cave, China<sup>27</sup> and isotope records from  
177 Greenland Summit ice cores<sup>30</sup> (Supplementary Fig. 1). The rationale for this correlation rests on the close  
178 relationship between Greenland temperatures, North Atlantic Ocean temperature and circulation, and the  
179 Asian Monsoon on decadal to millennial time scales<sup>22–25</sup>.

180 For the correlation we used the MS record of core GS07-148-17GC determined in 2 mm steps by a  
181 Geotek<sup>TM</sup> multi sensor core logger and a Barlington2 point sensor. MS in Norwegian Sea sediments is  
182 considered to be a proxy for the strength of the warm Atlantic Water inflow over the basaltic Iceland Scot-  
183 land Ridge through ocean current erosion and transport of magnetic mineral grains that are subsequently  
184 deposited in the S-Norwegian sea; the Atlantic water inflow is in turn tightly linked to the general North  
185 Atlantic climate, including Greenland temperatures<sup>33,65–67</sup>.

186 We used the Hulu cave speleothem H82  $\delta^{18}\text{O}$  record as the Norwegian Sea MS correlation target be-  
187 cause of its high temporal resolution, and because it contains high-amplitude signals that covary with the  
188 MS record. This covariance has been attributed to fast atmospheric teleconnections between ocean circula-  
189 tion in the North Atlantic and regional Asian monsoon intensity and isotopic fractionation captured in  
190 the speleothem  $\delta^{18}\text{O}$ <sup>23,68</sup>. The covariation between Greenland ice core  $\delta^{18}\text{O}$  and Norwegian sea MS is  
191 more subdued, especially during Heinrich Stadial 1 (HS1), which has been attributed to a diminishing ef-  
192 fect of North Atlantic circulation on Greenland temperatures during cold intervals<sup>69</sup>. The Hulu Cave H82  
193 chronology rests solidly on a large number of U/Th dates that, paired with AMS  $^{14}\text{C}$  measurements, yield  
194 a high-resolution time series of atmospheric  $^{14}\text{C}$  ages<sup>27</sup>, which forms the backbone of the IntCal13 atmo-  
195 spheric radiocarbon reconstruction<sup>29</sup>. By tying our Norwegian Sea  $^{14}\text{C}$  record directly to the Hulu Cave  
196  $\delta^{18}\text{O}$ , we operate on the same absolute time scale as IntCal13. Hence, we can determine the reservoir age  
197 effect in the Norwegian Sea (the difference between the IntCal13 atmospheric  $^{14}\text{C}$  ages and the Norwegian  
198 Sea  $^{14}\text{C}$  ages). This approach is more precise than tying the Norwegian Sea record to the Greenland ice  
199 core chronology (GICC05)<sup>70</sup>, which has a cumulative counting error of up to  $\pm 400$  yr in the time interval  
200 considered here.

201 The GS07-148-17GC age model was constructed using the Oxcal v4.3.2 software<sup>62</sup>, and the P\_Sequence  
202 sediment deposition model<sup>63</sup> with the variable  $k$  option<sup>64</sup>. The age-uncertainty for each tie-point was de-  
203 rived from a Oxcal P\_Sequence model of the H82 speleothem, using the U/Th dates from Ref.<sup>27</sup> (Supple-  
204 mentary Fig. 1). To account for uncertainty in the lead-lag relationships between the records, we assume  
205 an added uncertainty of  $\pm 25$  yr ( $1\sigma$ ) to each tie-point. Although the correlation depicted in Supplementary  
206 Fig. 1 is very detailed, the resulting age-depth relationship for the Norwegian Sea cores remains smooth  
207 and roughly linear between the Holocene boundary and an interval of rapid deposition centered at 17.5 ka  
208 that is related to the break-up of the Norwegian Channel Ice Stream<sup>71,72</sup> and a catastrophic drainage of a  
209 large ice dammed lake in the North Sea<sup>73</sup>. Our correlation is validated by the occurrence of the Vedde Ash  
210 layer in the interval ascribed to Younger Dryas both in the GS07-148-17GC and in the Greenland ice core  
211 records<sup>30</sup> (Supplementary Fig. 1).

212 To assess the sensitivity of our results to the reconstructed chronology, we explored an alternative depo-  
213 sition model without any assumptions of teleconnections or synchrony between proxy records (Supplemen-  
214 tary Fig. 2). We constrained the ages of this alternative model with the Vedde Ash, which is dated by layer  
215 counting in the Greenland ice cores to  $12121 \pm 57$  cal yr BP on the GICC05 chronology<sup>74</sup> (Supplementary  
216 Fig. 1), and with 24  $^{14}\text{C}$  dates from our compilation (Supplementary data file). We restricted the use of  
217  $^{14}\text{C}$  dates to the Younger Dryas and Bølling-Allerød time periods where the Norwegian Sea  $R$  has been  
218 independently constrained by paired marine and terrestrial  $^{14}\text{C}$  dates<sup>75</sup>. We then used the *Marine13* cali-  
219 bration curve<sup>29</sup> with a  $\Delta R$  of  $100 \pm 50$  yr, and the same depositional model as in our preferred chronology,  
220 invoking the default *general* outlier model<sup>76</sup>. Due to a lack of pre-Bølling age constraints, this alterna-  
221 tive chronology expectedly shows much greater pre-Bølling age uncertainty than our preferred chronology.  
222 Nevertheless, the two chronologies overlap almost entirely in their 68.2 % ( $1\sigma$ ) credible intervals (Supple-  
223 mentary Fig. 2). Notably, the alternative chronology yields a drop in  $^{14}\text{C}$  age at the Bølling transition that is  
224 steeper than in our preferred chronology, implying an even more abrupt EIS collapse. Hence, we conclude  
225 that the inferred drop in  $R$  at the Bølling transition is unlikely to be an artefact of the age model, and that  
226 our estimates are conservative in terms of the rate of EIS mass loss and its contribution to the MWP-1a.

227 From the compiled time series of  $^{14}\text{C}$  ages we calculate  $R$  as the difference between the Norwegian Sea  
228  $^{14}\text{C}$  and the *Intcal13* atmospheric  $^{14}\text{C}$  calibration curve<sup>29</sup> (Fig. 2F). To incorporate the uncertainty in both  
229 calendar ages and  $^{14}\text{C}$  ages in our reconstructed  $^{14}\text{C}$  and  $R$  record, we generated an uncertainty envelope

230 by Monte Carlo sampling of multiple posterior probability density functions (PDFs) generated by the Oxcal  
231 sediment deposition models of the core stratigraphies: (i) PDFs of the stratigraphic alignment of the four  
232 Norwegian Sea sediment cores, (ii) PDFs of the depositional model for the GS07-148-17GC core, which  
233 incorporate both the uncertainty in the Hulu Cave target  $\delta^{18}\text{O}$  record and uncertainty in the correlation to  
234 the Hulu Cave record, and (iii) PDFs of the  $^{14}\text{C}$  measurements. Our time series of  $^{14}\text{C}$  ages is the mean  
235  $\pm 1\sigma$  of  $10^5$  Monte Carlo realizations of the dataset in 10-yr bins using linear interpolation. It spans the  
236 period from 12,200 to 19,000 cal yr BP and is available as supplementary data formatted as a .14c file that  
237 can be used directly in radiocarbon calibration software.

238 Our  $R$  record are consistent with  $R$  values previously reported from the North Atlantic and the Norwe-  
239 gian Sea and coast<sup>34,75,77–79</sup>. Although a different approach was used to constrain the calendar ages of core  
240 GIK23074<sup>34</sup>, we arrive at similar reservoir ages.

## 241 Tephrochronology

242 Tephra shards were quantified in the  $>100\ \mu\text{m}$  grain fraction in  $\sim 20$  cm interval of core GS07-148-17GC  
243 corresponding to the Younger Dryas chronozone. This interval was chosen with the aim of finding the  
244 Vedde Ash tephra that is a key chronostratigraphic marker horizon in the North Atlantic region, and is also  
245 found in the Greenland Ice cores<sup>30</sup> and several of the Norwegian Sea cores used in this study<sup>32,33</sup>. Based on  
246 their colour and morphological character, tephra particles were grouped into a transparent-white rhyolitic  
247 type of tephra and a brown basaltic type of tephra. The total count from each of these tephra types was  
248 normalized using the total dry weight of the samples and the results plotted versus depth (Supplementary  
249 Fig. 1)

250 Tephra shards from three depth intervals (32.5-33.0, 33.5-34.0 and 36.0-36.5 cm) were selected for geo-  
251 chemical analysis. 25-30 shards of both rhyolitic and basaltic type were picked for major oxide geochemical  
252 analysis on the University of Bergen Zeiss Supra 55 VP scanning electron microscope. The microscope was  
253 attached to a Thermo energy dispersive X-ray spectrometer with 9.5 mm working distance, beam current  
254 of 1.00 mA, an aperture size of  $60\ \mu\text{m}$ , beam width of  $6\ \mu\text{m}$  and detection time of 60 s. The results are  
255 presented in the Supplementary Data File and in Supplementary Fig. 3. As the geochemical analysis were  
256 performed directly on the shards and without any leveling or polishing the beam will hit the surface from  
257 different angles. This resulted in that the counting rate of the different elements becomes slightly more  
258 scattered than during analysis on a polished thin section. The major element composition is, however,  
259 consistent with published major element data from the Vedde Ash (Supplementary Fig. 3).

## 260 Ice sheet margin reconstructions

261 We reconstructed the deglaciation of the EIS complex in a Bayesian chronological framework using Oxcal  
262 4.2.4<sup>62–64,76</sup>. The prior model was constructed using available chronological, stratigraphical and morpho-  
263 logical data that were aggregated, independently for the BSIS and the FIS, into a sequence of phases with  
264 known relative ages. A phase in this context refers to the retreat (or advance) of the ice sheet in a specific  
265 area.

266 We grouped the deglaciation of the FIS ice sheet into two phases: (i) late HS1 advance and (ii) deglacia-  
267 tion on the continental shelf and outer coasts. Following the deglaciation of the continental shelf, we use the  
268 ages and ice sheet geometries provided by the *Dated-1* reconstruction<sup>19</sup> in the 14-10 ka interval, as these  
269 are predominantly based on terrestrial dates not affected by our recalibration of the marine  $^{14}\text{C}$  dates. The  
270 ice margins along the southern and eastern margins of the FIS were generated by interpolating between the  
271 15 ka and 14 ka *Dated-1* ice margins using the TopoToRaster tool in ArcMap 10.5.1. On the Norwegian  
272 continental shelf, evidence suggests that the deeper troughs deglaciated rapidly compared to the shallower  
273 banks<sup>80–82</sup>.

274 The more complex deglaciation history of the BSIS was divided into five phases: (i) late HS1 advance,  
275 (ii) deglaciation of the major overdeepened areas of Storfjorden trough, Bear Island trough and Franz Vic-  
276 toria trough, and the narrow continental shelf areas west and north of Svalbard, (iii) deglaciation of the  
277 Central Deep, (iv) final deglaciation of the shallow banks in the northern Barents Sea, and (v) ice retreat  
278 to the Svalbard archipelago. An early deglacial phase was added before the late HS1 advance, without  
279 assigning ice sheet margins. At 12-10 ka we used the *Dated-1*<sup>19</sup> BSIS ice sheet geometries.

280 We adapt a previously proposed ice sheet retreat pattern for the southern Barents Sea, suggesting  
281 episodic rapid retreat in the Bear Island trough<sup>83–87</sup>. Well preserved retreat ridges suggest that the ice  
282 remaining on the shallower banks retreated more slowly<sup>85</sup>. The final ice movement on the southern Barents

283 sea banks was from the east<sup>85,87</sup> suggesting an ice dome remained over the Central Deep following the  
284 separation of the BSIS and the FIS (Fig. 1).

285 The age-control of each phase was constrained by the ages of sediment facies and/or facies transitions  
286 linked to ice margin positions within the phase (Supplementary Figs. 7 and 8), as well as by the age  
287 information of adjacent phases in the sequence. We used the published <sup>14</sup>C dates either directly as ages of  
288 the sampled sedimentary units, or, in cases where sufficient published dates and stratigraphic information  
289 were available, used PDFs of sediment unit boundaries (e.g. the boundary between subglacial till and  
290 glacial-proximal sedimentary facies) generated with the OxCal P\_Sequence deposition model<sup>63,64</sup>. Outliers  
291 were detected and dealt with using the default *general* outlier model in Oxcal<sup>76</sup> (Supplementary Figs. 7;8).  
292 To account for possible deviations in  $R$  from the reconstructed Norwegian Sea <sup>14</sup>C and Marine13, we  
293 add a  $\Delta R$  of  $0 \pm 50$  <sup>14</sup>C years ( $1 \sigma$ ) to each marine radiocarbon age determination. To calibrate marine  
294 conventional <sup>14</sup>C ages younger than 11800 <sup>14</sup>C years, we use the Marine13 curve<sup>29</sup>, terrestrial dates are  
295 calibrated with the IntCal13<sup>29</sup>.

296 For each phase of the deglaciation we outlined a succession of ice margins (Fig. 1) based on published  
297 sediment core data, geomorphological interpretations and ice sheet reconstructions for the BSIS<sup>19,21,48,83–122</sup>  
298 and FIS<sup>19,42,47,72,73,80–82,111,123–136</sup>. The available information is, however, too sparse to yield continuous  
299 time-synchronous margins and we stress that the reconstructed margins are intended to capture the general  
300 pattern of retreat rather than to be accurate representation of the ice sheet at a specific time. To account for  
301 uncertainty in the ice sheet geometry, we follow the approach of<sup>19</sup> and construct accompanying maximum  
302 and minimum margins (Fig. 1). These are treated as the 95% quantiles. For margins derived from the  
303 *Dated-1* reconstruction, we use their max and min margins<sup>19</sup>.

## 304 Ice sheet volume estimates

305 We converted the reconstructed ice sheet areas to volumes using the approximation proposed by Paterson<sup>37</sup>:  
306  $\log V = 1.23(\log S - 1)$ , where  $V$  is volume and  $S$  is area. Paterson's formula was determined empirically  
307 by regression of measurements on six extant ice sheets and ice caps, the boundary conditions of which  
308 are not directly comparable to those of the EIS. To assess the sensitivity of the volume estimates to the  
309 regression assumptions, we also used the area-volume relationships from the output of a recent ice-sheet  
310 model of the EIS<sup>38</sup> to convert the reconstructed areas volume (Supplementary Fig. 9). Although the model-  
311 based regression yields an EIS volume that is 2.7 m SLE smaller than the Paterson approximation at the  
312 start of the deglaciation, the difference in the estimated ice loss between 14.7 and 14.4 kyr BP is only ~0.2  
313 m SLE, which is negligible with respect to our conclusions (Supplementary Fig. 9). Paleo-depths of the  
314 continental shelves on which the EIS was grounded are obscured by an unknown amount of isostatic uplift  
315 since deglaciation. Without correcting for ice volume below flotation through glacio-isostatic modelling,  
316 which is outside the scope of our study, our estimated volumes cannot be interpreted as eustatic sea-level  
317 change. For each ice sheet margin reconstruction and associated uncertainty estimates, we generated a  
318 PDF of the volume estimate using Gaussian kernels. The volume-PDF and accompanying age-PDF of each  
319 reconstructed ice sheet were resampled using a Monte Carlo technique detailed at <https://github.com/kahaaga/EurasianDeglaciation>.  
320

## 321 The effect of bioturbation

322 The Norwegian Sea sediment core GS07-148-17GC (Fig. 1) features a large, complex burrow with open  
323 cavities containing pellets (Supplementary Fig. 5). Unlike ambient biogenic sediment mixing, which is  
324 typically limited to an upper mixed layer, this burrow (or set of burrows) extends ~25 cm down into the  
325 late HS1, and may have transported younger material down through this stratigraphic interval. Seven <sup>14</sup>C  
326 dates from this interval of the GS07-148-17GC core deviate from the ages in nearby cores GIK23074 and  
327 HM79-6 (Fig. 1) at the same stratigraphic level. The presence of the large burrow through this interval  
328 compelled us to discard these <sup>14</sup>C dates from the <sup>14</sup>C reconstruction (Supplementary Fig. 4).

329 To assess the potential impact of ambient biogenic sediment mixing on the observed decline in  $R$  at  
330 the Bølling transition, we used the TURBO2 model<sup>137</sup>, a mixed layer model with instantaneous mixing  
331 designed to simulate the effects of bioturbation on proxy records from sedimentary particles such as  
332 foraminifera. As input we used 1,024 simulated vectors of abundance generated as normally distributed  
333 random values centered on the best-fit linear trend and with the standard deviation of the observed record  
334 of the abundance of foraminifera from the MD95-2010 core<sup>33</sup>. The simulated number of specimens picked  
335 for measurement was set to 200. To focus on the change in  $R$  across the Bølling transition, we limited the  
336 modeling to the time interval between ~15,400 and ~13,700 calendar yr BP. To keep the model as simple

337 as possible, we let the hypothetical true decline in  $R$  be an instantaneous step change superimposed on the  
338 overall linear trend in the observed  $^{14}\text{C}$  record, and we assumed a constant mixed layer depth. Under this  
339 scenario, if we invoked a drop in the modeled  $R$  record of  $\sim 1,220$   $^{14}\text{C}$  yr from 14,600 to 14,550 calendar yr  
340 BP and used a mixed layer depth of 6 cm, then the bioturbated  $^{14}\text{C}$  ages simulated by TURBO2 provided a  
341 reasonable fit to the observed  $^{14}\text{C}$  record (Supplementary Fig. 6). Hence, the effect of bioturbation would  
342 be to temporally smear out a more abrupt event in the  $^{14}\text{C}$  record. This smearing effect pushes the recalibrated  
343  $^{14}\text{C}$  ages for the start of the deglaciation backwards in time, and attenuates the estimated EIS melt  
344 water flux. An upward bias towards older ages affects  $^{14}\text{C}$  dates between  $\sim 13,200$  and  $14,000$   $^{14}\text{C}$  yr BP in  
345 particular, and is important to bear in mind if the  $^{14}\text{C}$  record is to be used as a regional calibration curve.

## 346 Acknowledgements

347 This work is funded by the Research Council of Norway through grants no. 221999 (JB) and 231259 (BH),  
348 and by the Bergen Research Foundation (BH). JB was also supported through the RISES project of the  
349 Centre for Climate Dynamics at the Bjerknes Centre for Climate Research. Additional support was received  
350 from JSPS KAKENHI 17H01168 and 15KK0151 (YY). JB, HH, KAH and BH acknowledge discussions  
351 with colleagues at the department of Earth Science and the Bjerknes Centre for Climate Research at the  
352 University of Bergen. We thank the captain and crew of R/V G.O. Sars for retrieving Core GS07-148-  
353 17GC. Salad Yusuf Ali, Kristin Flesland and Eivind N. Støren is thanked for technical support.

## 354 Author contributions

355 J.B. conceived and designed the study, developed the core chronology, the deglaciation chronology, and  
356 the ice margin reconstruction. H.H. collected sediment core GS07-148-17GC and performed tephrochronological  
357 and geochemical analyses. Y. Y. performed AMS  $^{14}\text{C}$  analyses. K. A. H. and J.B. developed the  
358 Norwegian Sea  $^{14}\text{C}$  reconstruction and performed statistical analyses. B. H. performed bioturbation mod-  
359 elling. J.B., B.H. and K. A. H. wrote the paper, and all authors contributed to the writing of the final version  
360 of the manuscript.

## 361 References

- 362 [1] Stocker, T. *Climate change 2013: the physical science basis: Working Group I contribution to the*  
363 *Fifth assessment report of the Intergovernmental Panel on Climate Change* (Cambridge University  
364 Press, 2014).
- 365 [2] Fairbanks, R. G. A 17,000-year glacio-eustatic sea level record: influence of glacial melting rates on  
366 the Younger Dryas event and deep-ocean circulation. *Nature* **342**, 637–642 (1989).
- 367 [3] Blanchon, P. & Shaw, J. Reef drowning during the last deglaciation: Evidence for catastrophic  
368 sea-level rise and ice-sheet collapse. *Geology* **23**, 4 (1995). URL [+http://dx.doi.org/10.1130/0091-7613\(1995\)023\(023\)3C0004:RDDTLD\(%\)3E2.3.CO;2](http://dx.doi.org/10.1130/0091-7613(1995)023(023)3C0004:RDDTLD(%)3E2.3.CO;2).
- 369 [4] Hanebuth, T., Statterger, K. & Grootes, P. M. Rapid flooding of the Sunda Shelf: a late-glacial  
370 sea-level record. *Science* **288**, 1033–1035 (2000).
- 371 [5] Deschamps, P. *et al.* Ice-sheet collapse and sea-level rise at the Bolling warming 14,600 years ago.  
372 *Nature* **483**, 559–564 (2012).
- 373 [6] Liu, J., Milne, G. A., Kopp, R. E., Clark, P. U. & Shennan, I. Sea-level constraints on the amplitude  
374 and source distribution of meltwater pulse 1a. *Nature Geoscience* **9**, 130 (2016).
- 375 [7] Bassett, S. E., Milne, G. A., Mitrovica, J. X. & Clark, P. U. Ice sheet and solid earth influences on  
376 far-field sea-level histories. *Science* **309**, 925–928 (2005).
- 377 [8] Clark, P. U. *et al.* Origin of the first global meltwater pulse following the last glacial maximum.  
378 *Paleoceanography* **11**, 563–577 (1996).
- 379 [9] Clark, P. U., Mitrovica, J., Milne, G. & Tamisiea, M. Sea-level fingerprinting as a direct test for the  
380 source of global meltwater pulse 1a. *Science* **295**, 2438–2441 (2002).
- 381

- 382 [10] Carlson, A. E. & Clark, P. U. Ice sheet sources of sea level rise and freshwater discharge  
383 during the last deglaciation. *Reviews of Geophysics* **50** (2012). URL [https://agupubs.  
onlinelibrary.wiley.com/doi/abs/10.1029/2011RG000371](https://agupubs.<br/>384 onlinelibrary.wiley.com/doi/abs/10.1029/2011RG000371).
- 385 [11] McManus, J. F., Francois, R., Gherardi, J.-M., Keigwin, L. D. & Brown-Leger, S. Collapse and rapid  
386 resumption of Atlantic meridional circulation linked to deglacial climate changes. *Nature* **428**, 834  
387 (2004).
- 388 [12] Stanford, J., Rohling, E., Bacon, S. & Holliday, N. A review of the deep and surface currents around  
389 eirik drift, south of greenland: Comparison of the past with the present. *Global and Planetary  
390 Change* **79**, 244–254 (2011).
- 391 [13] Weertman, J. Stability of the junction of an ice sheet and an ice shelf. *Journal of Glaciology* **13**,  
392 3–11 (1974).
- 393 [14] Mercer, J. H. West Antarctic ice sheet and CO<sub>2</sub> greenhouse effect: a threat of disaster. *Nature* **271**,  
394 321 (1978).
- 395 [15] Hughes, T. J. The weak underbelly of the West Antarctic ice sheet. *Journal of Glaciology* **27**,  
396 518–525 (1981).
- 397 [16] Joughin, I., Smith, B. E. & Medley, B. Marine ice sheet collapse potentially under way for the  
398 Thwaites Glacier Basin, West Antarctica. *Science* **344**, 735–738 (2014).
- 399 [17] Ritz, C. *et al.* Potential sea-level rise from Antarctic ice-sheet instability constrained by observations.  
400 *Nature* **528**, 115 (2015).
- 401 [18] DeConto, R. M. & Pollard, D. Contribution of Antarctica to past and future sea-level rise. *Nature*  
402 **531**, 591 (2016).
- 403 [19] Hughes, A. L. C., Gyllencreutz, R., Lohne, Ø. S., Mangerud, J. & Svendsen, J. I. The last Eurasian  
404 ice sheets – a chronological database and time-slice reconstruction, DATED-1. *Boreas* **45**, 1–45  
405 (2016). URL <http://dx.doi.org/10.1111/bor.12142>.
- 406 [20] Stouffer, R. J. *et al.* Investigating the causes of the response of the thermohaline circulation to past  
407 and future climate changes. *Journal of Climate* **19**, 1365–1387 (2006).
- 408 [21] Hormes, A., Gjermundsen, E. F. & Rasmussen, T. L. From mountain top to the deep sea—Deglaciation  
409 in 4D of the northwestern Barents Sea ice sheet. *Quaternary Science Reviews* **75**, 78–99 (2013).
- 410 [22] Wang, Y. J. *et al.* A High-Resolution Absolute-Dated Late Pleistocene Monsoon Record from Hulu  
411 Cave, China. *Science* **294**, 2345–2348 (2001). URL [http://science.sciencemag.org/  
content/294/5550/2345](http://science.sciencemag.org/<br/>412 content/294/5550/2345).
- 413 [23] Orland, I. J. *et al.* Direct measurements of deglacial monsoon strength in a Chinese stalagmite.  
414 *Geology* **43**, 555 (2015). URL [+http://dx.doi.org/10.1130/G36612.1](http://dx.doi.org/10.1130/G36612.1).
- 415 [24] Cheng, H. *et al.* Ice Age Terminations. *Science* **326**, 248–252 (2009). URL [http://science.  
sciencemag.org/content/326/5950/248](http://science.<br/>416 sciencemag.org/content/326/5950/248).
- 417 [25] Deplazes, G. *et al.* Links between tropical rainfall and North Atlantic climate during the last glacial  
418 period. *Nature Geoscience* **6**, 213 (2013).
- 419 [26] Hughen, K., Southon, J., Lehman, S., Bertrand, C. & Turnbull, J. Marine-derived <sup>14</sup>C calibration  
420 and activity record for the past 50,000 years updated from the Cariaco Basin. *Quaternary Science  
421 Reviews* **25**, 3216–3227 (2006).
- 422 [27] Southon, J., Noronha, A. L., Cheng, H., Edwards, R. L. & Wang, Y. A high-resolution record of  
423 atmospheric <sup>14</sup>C based on Hulu Cave speleothem H82. *Quaternary Science Reviews* **33**, 32–41  
424 (2012).
- 425 [28] Wu, J., Wang, Y., Cheng, H. & Edwards, L. R. An exceptionally strengthened East Asian summer  
426 monsoon event between 19.9 and 17.1 ka BP recorded in a Hulu stalagmite. *Science in  
427 China Series D: Earth Sciences* **52**, 360–368 (2009). URL [https://doi.org/10.1007/  
s11430-009-0031-1](https://doi.org/10.1007/<br/>428 s11430-009-0031-1).

- 429 [29] Reimer, P. J. *et al.* IntCal13 and Marine13 radiocarbon age calibration curves 0–50,000 years cal BP.  
430 *Radiocarbon* **55**, 1869–1887 (2013).
- 431 [30] Seierstad, I. K. *et al.* Consistently dated records from the Greenland GRIP, GISP2 and NGRIP ice  
432 cores for the past 104ka reveal regional millennial-scale  $\delta^{18}\text{O}$  gradients with possible Heinrich event  
433 imprint. *Quaternary Science Reviews* **106**, 29–46 (2014). URL <http://www.sciencedirect.com/science/article/pii/S027737911400434X>.  
434
- 435 [31] Voelker, A. H. L. *Zur Deutung der Dansgaard-Oeschger Ereignisse in ultra-hochauflösenden*  
436 *Sedimentprofilen aus dem Europäischen Nordmeer*. Ph.D. thesis, Institut für Geowissenschaften,  
437 Christian-Albrechts-Universität (1999).
- 438 [32] Karpuz, N. K. & Jansen, E. A high-resolution diatom record of the last deglaciation from the SE  
439 Norwegian Sea: Documentation of rapid climatic changes. *Paleoceanography* **7**, 499–520 (1992).  
440 URL <http://dx.doi.org/10.1029/92PA01651>.
- 441 [33] Dokken, T. M. & Jansen, E. Rapid changes in the mechanism of ocean convection during the last  
442 glacial period. *Nature* **401**, 458–461 (1999).
- 443 [34] Sarnthein, M., Balmer, S., Grootes, P. M. & Mudelsee, M. Planktic and benthic  $^{14}\text{C}$  reservoir ages  
444 for three ocean basins, calibrated by a suite of  $^{14}\text{C}$  plateaus in the glacial-to-deglacial Suigetsu at-  
445 mospheric  $^{14}\text{C}$  record. *Radiocarbon* **57**, 129–151 (2015).
- 446 [35] Dreger, D. *Decadal to Centennial Scale Sediment Records of Ice Advance on the Barents Shelf and*  
447 *Meltwater Discharge Into the Northeastern Norwegian Sea Over the Last 40 Kyr: Dekadische Bis*  
448 *Jahrhundert-Variabilität Von Eisvorstößen Auf Dem Barentsschelf und Schmelzwasserschüben in Die*  
449 *Nordöstliche Norwegensee Während Der Letzten 40 Ka*. Ph.D. thesis, Inst. für Geowiss. (1999).
- 450 [36] Sarnthein, M. *et al.* Fundamental modes and abrupt changes in North Atlantic circulation and climate  
451 over the last 60 ky—Concepts, reconstruction and numerical modeling. In *The Northern North*  
452 *Atlantic*, 365–410 (Springer, 2001).
- 453 [37] Paterson, W. S. B. Laurentide Ice Sheet: estimated volumes during late Wisconsin. *Reviews of*  
454 *Geophysics* **10**, 885–917 (1972).
- 455 [38] Patton, H. *et al.* Deglaciation of the Eurasian ice sheet complex. *Quaternary Science Reviews* **169**,  
456 148–172 (2017). URL <http://www.sciencedirect.com/science/article/pii/S0277379117302068>.  
457
- 458 [39] Gregoire, L. J., Otto-Bliesner, B., Valdes, P. J. & Ivanovic, R. Abrupt bølling warming and ice saddle  
459 collapse contributions to the meltwater pulse 1a rapid sea level rise. *Geophysical research letters* **43**,  
460 9130–9137 (2016).
- 461 [40] Tarasov, L., Dyke, A. S., Neal, R. M. & Peltier, W. R. A data-calibrated distribution of deglacial  
462 chronologies for the north american ice complex from glaciological modeling. *Earth and Planetary*  
463 *Science Letters* **315**, 30–40 (2012).
- 464 [41] Shennan, I. *et al.* Relative sea-level changes, glacial isostatic modelling and ice-sheet reconstructions  
465 from the british isles since the last glacial maximum. *Journal of Quaternary Science: Published for*  
466 *the Quaternary Research Association* **21**, 585–599 (2006).
- 467 [42] Romundset, A., Bondevik, S. & Bennike, O. Postglacial uplift and relative sea level changes in  
468 Finnmark, northern Norway. *Quaternary Science Reviews* **30**, 2398–2421 (2011).
- 469 [43] Lohne, Ø. S., Bondevik, S., Mangerud, J. & Svendsen, J. I. Sea-level fluctuations imply that the  
470 younger dryas ice-sheet expansion in western norway commenced during the allerød. *Quaternary*  
471 *Science Reviews* **26**, 2128–2151 (2007).
- 472 [44] Svendsen, J. I. & Mangerud, J. Late weichselian and holocene sea-level history for a cross-section  
473 of western norway. *Journal of Quaternary Science* **2**, 113–132 (1987).
- 474 [45] Bentley, M. J. *et al.* A community-based geological reconstruction of antarctic ice sheet deglaciation  
475 since the last glacial maximum. *Quaternary Science Reviews* **100**, 1–9 (2014).

- 476 [46] Buizert, C. *et al.* Greenland temperature response to climate forcing during the last deglaciation.  
477 *Science* **345**, 1177–1180 (2014).
- 478 [47] Hafidason, H., Sejrup, H. P., Kristensen, D. K. & Johnsen, S. Coupled response of the late glacial  
479 climatic shifts of northwest Europe reflected in Greenland ice cores: Evidence from the northern  
480 North Sea. *Geology* **23**, 1059–1062 (1995).
- 481 [48] Rasmussen, T. L. *et al.* Paleoceanographic evolution of the SW Svalbard margin (76 N) since 20,000  
482 <sup>14</sup>C yr BP. *Quaternary Research* **67**, 100–114 (2007).
- 483 [49] Jenkins, A. *et al.* Observations beneath pine island glacier in west antarctica and implications for its  
484 retreat. *Nature Geoscience* **3**, 468 (2010).
- 485 [50] Jacobs, S. S., Jenkins, A., Giulivi, C. F. & Dutrieux, P. Stronger ocean circulation and increased  
486 melting under pine island glacier ice shelf. *Nature Geoscience* **4**, 519 (2011).
- 487 [51] Yokoyama, Y. *et al.* Widespread collapse of the ross ice shelf during the late holocene. *Proceedings*  
488 *of the National Academy of Sciences* **113**, 2354–2359 (2016).
- 489 [52] Piasecka, E. D., Stokes, C. R., Winsborrow, M. C. & Andreassen, K. Relationship between mega-  
490 scale glacial lineations and iceberg ploughmarks on the bjørnøyrenna palaeo-ice stream bed, barents  
491 sea. *Marine Geology* **402**, 153–164 (2018).
- 492 [53] Pollard, D., DeConto, R. M. & Alley, R. B. Potential antarctic ice sheet retreat driven by hydrofrac-  
493 turing and ice cliff failure. *Earth and Planetary Science Letters* **412**, 112–121 (2015).
- 494 [54] Wise, M. G., Dowdeswell, J. A., Jakobsson, M. & Larter, R. D. Evidence of marine ice-cliff insta-  
495 bility in pine island bay from iceberg-keel plough marks. *Nature* **550**, 506 (2017).
- 496 [55] Howell, D., Siegert, M. J. & Dowdeswell, J. A. Modelling the influence of glacial isostasy on late  
497 weichselian ice-sheet growth in the barents sea. *Journal of Quaternary Science: Published for the*  
498 *Quaternary Research Association* **15**, 475–486 (2000).
- 499 [56] Edwards, T. L. *et al.* Revisiting antarctic ice loss due to marine ice-cliff instability. *Nature* **566**, 58  
500 (2019).
- 501 [57] Ng, H. C. *et al.* Coherent deglacial changes in western atlantic ocean circulation. *Nature communi-*  
502 *cations* **9** (2018).
- 503 [58] Condron, A. & Winsor, P. Meltwater routing and the younger dryas. *Proceedings of the National*  
504 *Academy of Sciences* **109**, 19928–19933 (2012).
- 505 [59] Yokoyama, Y., Miyairi, Y., Matsuzaki, H. & Tsunomori, F. Relation between acid dissolution time  
506 in the vacuum test tube and time required for graphitization for ams target preparation. *Nuclear*  
507 *Instruments and Methods in Physics Research Section B: Beam Interactions with Materials and*  
508 *Atoms* **259**, 330–334 (2007).
- 509 [60] Yokoyama, Y., Koizumi, M., Matsuzaki, H., Miyairi, Y. & Ohkouchi, N. Developing ultra small-scale  
510 radiocarbon sample measurement at the university of tokyo. *Radiocarbon* **52**, 310–318 (2010).
- 511 [61] Yokoyama, Y. *et al.* A single stage accelerator mass spectrometry at the atmosphere and ocean  
512 research institute, the university of tokyo. *Nuclear Instruments and Methods in Physics Research*  
513 *Section B* (2018).
- 514 [62] Bronk Ramsey, C. Bayesian analysis of radiocarbon dates. *Radiocarbon* **51**, 337–360 (2009).
- 515 [63] Bronk Ramsey, C. Deposition models for chronological records. *Quaternary Science Reviews* **27**,  
516 42–60 (2008).
- 517 [64] Bronk Ramsey, C. & Lee, S. Recent and planned developments of the program OxCal. *Radiocarbon*  
518 **55**, 720–730 (2013).
- 519 [65] Rasmussen, T. L., van Weering, T. C. E. & Labeyrie, L. Climatic instability, ice sheets and ocean  
520 dynamics at high northern latitudes during the last glacial period (58-10 KA BP). *Quaternary Science*  
521 *Reviews* **16**, 71–80 (1997). URL [http://www.sciencedirect.com/science/article/  
522 pii/S0277379196000455](http://www.sciencedirect.com/science/article/pii/S0277379196000455).

- 523 [66] Kissel, C. *et al.* Rapid climatic variations during marine isotopic stage 3: magnetic analysis  
524 of sediments from Nordic Seas and North Atlantic. *Earth and Planetary Science Letters* **171**,  
525 489–502 (1999). URL [http://www.sciencedirect.com/science/article/pii/  
526 S0012821X99001624](http://www.sciencedirect.com/science/article/pii/S0012821X99001624).
- 527 [67] Ballini, M., Kissel, C., Colin, C. & Richter, T. Deep-water mass source and dynamic associated with  
528 rapid climatic variations during the last glacial stage in the North Atlantic: A multiproxy investigation  
529 of the detrital fraction of deep-sea sediments. *Geochemistry, Geophysics, Geosystems* **7**, n/a—n/a  
530 (2006). URL <http://dx.doi.org/10.1029/2005GC001070>.
- 531 [68] Liu, Z. *et al.* Chinese cave records and the east asia summer monsoon. *Quaternary Science Reviews*  
532 **83**, 115–128 (2014).
- 533 [69] Landais, A. *et al.* Ice core evidence for decoupling between midlatitude atmospheric water cycle and  
534 greenland temperature during the last deglaciation. *Climate of the Past* **14**, 1405–1415 (2018).
- 535 [70] Andersen, K. K. *et al.* The greenland ice core chronology 2005, 15–42 ka. part 1: constructing the  
536 time scale. *Quaternary Science Reviews* **25**, 3246–3257 (2006).
- 537 [71] Hjelstuen, B. O. *et al.* Late quaternary seismic stratigraphy and geological development of the south  
538 vøring margin, norwegian sea. *Quaternary Science Reviews* **23**, 1847–1865 (2004).
- 539 [72] Lekens, W. A. H. *et al.* Laminated sediments preceding Heinrich event 1 in the Northern North  
540 Sea and Southern Norwegian Sea: Origin, processes and regional linkage. *Marine Geology*  
541 **216**, 27–50 (2005). URL [http://www.sciencedirect.com/science/article/pii/  
542 S0025322704003585](http://www.sciencedirect.com/science/article/pii/S0025322704003585).
- 543 [73] Hjelstuen, B. O., Sejrup, H. P., Valvik, E. & Becker, L. W. M. Evidence of an ice-dammed lake  
544 outburst in the North Sea during the last deglaciation. *Marine Geology* (2017).
- 545 [74] Rasmussen, S. O. *et al.* A new greenland ice core chronology for the last glacial termination. *Journal*  
546 *of Geophysical Research: Atmospheres* **111** (2006).
- 547 [75] Bondevik, S., Mangerud, J., Birks, H. H., Gulliksen, S. & Reimer, P. Changes in North Atlantic  
548 radiocarbon reservoir ages during the Allerød and Younger Dryas. *Science* **312**, 1514–1517 (2006).
- 549 [76] Bronk Ramsey, C. Dealing with outliers and offsets in radiocarbon dating. *Radiocarbon* **51**, 1023–  
550 1045 (2009).
- 551 [77] Waelbroeck, C. *et al.* The timing of the last deglaciation in North Atlantic climate records. *Nature*  
552 **412**, 724–727 (2001).
- 553 [78] Thornalley, D. J. R., McCave, I. N. & Elderfield, H. Tephra in deglacial ocean sediments south of  
554 Iceland: Stratigraphy, geochemistry and oceanic reservoir ages. *Journal of Quaternary Science* **26**,  
555 190–198 (2011). URL <http://dx.doi.org/10.1002/jqs.1442>.
- 556 [79] Stanford, J. D. *et al.* A new concept for the paleoceanographic evolution of Heinrich event 1 in  
557 the North Atlantic. *Quaternary Science Reviews* **30**, 1047–1066 (2011). URL [http://www.  
558 sciencedirect.com/science/article/pii/S0277379111000400](http://www.sciencedirect.com/science/article/pii/S0277379111000400).
- 559 [80] Dowdeswell, J. A., Ottesen, D., Evans, J., Cofaigh, C. Ó. & Anderson, J. B. Submarine glacial  
560 landforms and rates of ice-stream collapse. *Geology* **36**, 819 (2008). URL [+http://dx.doi.  
561 org/10.1130/G24808A.1](http://dx.doi.org/10.1130/G24808A.1).
- 562 [81] Rydningen, T. A., Vorren, T. O., Laberg, J. S. & Kolstad, V. The marine-based NW Fennoscandian  
563 ice sheet: glacial and deglacial dynamics as reconstructed from submarine landforms. *Quaternary*  
564 *Science Reviews* **68**, 126–141 (2013). URL [http://www.sciencedirect.com/science/  
565 article/pii/S027737911300067X](http://www.sciencedirect.com/science/article/pii/S027737911300067X).
- 566 [82] Brendryen, J. *et al.* Ice sheet dynamics on the Lofoten–Vesterålen shelf, north Norway, from Late  
567 MIS-3 to Heinrich Stadial 1. *Quaternary Science Reviews* **119**, 136–156 (2015). URL [http://  
568 www.sciencedirect.com/science/article/pii/S0277379115001225](http://www.sciencedirect.com/science/article/pii/S0277379115001225).

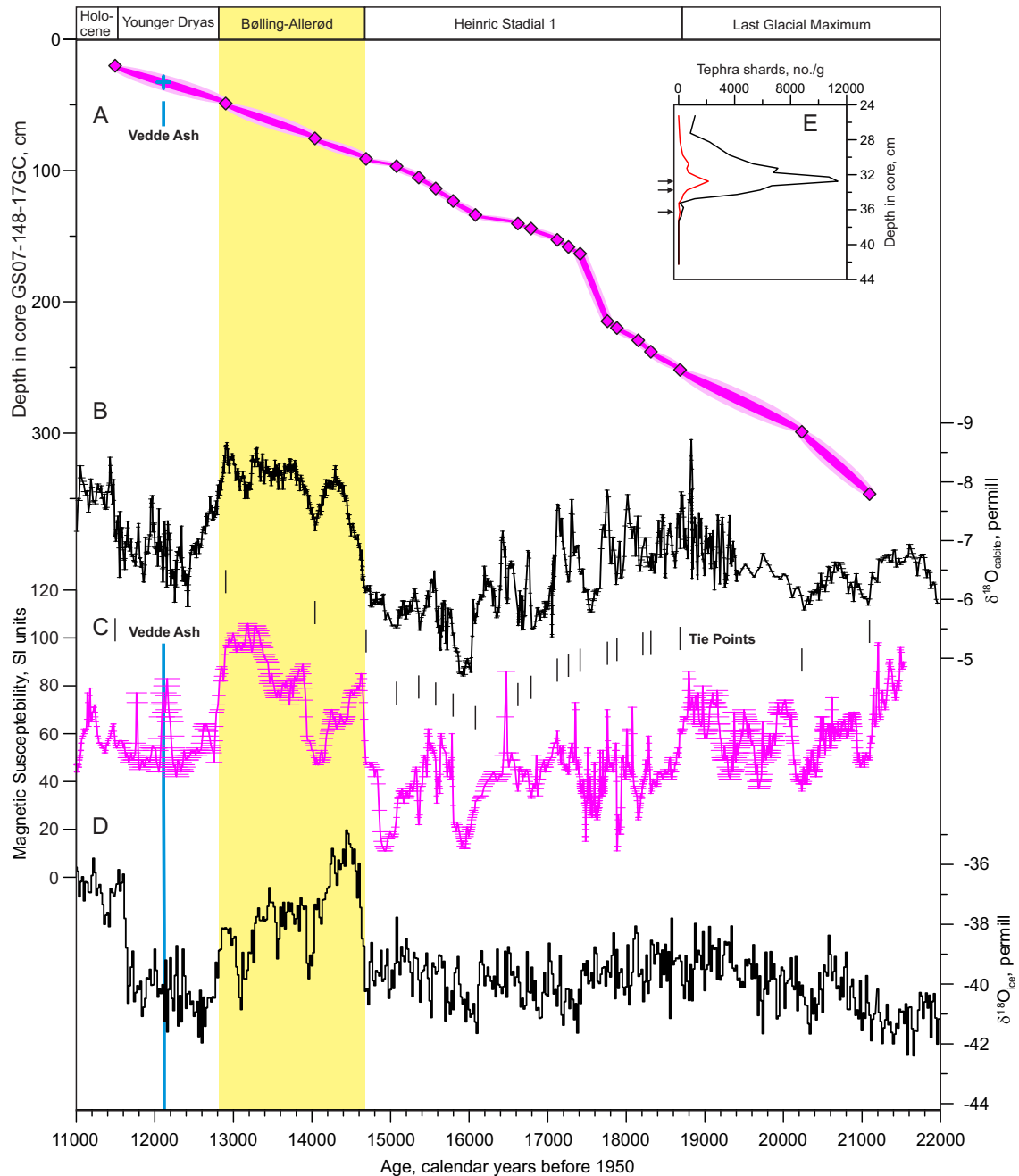
- 569 [83] Winsborrow, M. C. M., Andreassen, K., Corner, G. D. & Laberg, J. S. Deglaciation of a marine-  
570 based ice sheet: Late Weichselian palaeo-ice dynamics and retreat in the southern Barents Sea  
571 reconstructed from onshore and offshore glacial geomorphology. *Quaternary Science Reviews*  
572 **29**, 424–442 (2010). URL [http://www.sciencedirect.com/science/article/pii/  
573 S0277379109003333](http://www.sciencedirect.com/science/article/pii/S0277379109003333).
- 574 [84] Andreassen, K., Winsborrow, M. C. M., Bjarnadóttir, L. R. & Rüther, D. C. Ice stream retreat  
575 dynamics inferred from an assemblage of landforms in the northern Barents Sea. *Quaternary Science*  
576 *Reviews* **92**, 246–257 (2014).
- 577 [85] Bjarnadóttir, L. R., Winsborrow, M. C. M. & Andreassen, K. Deglaciation of the central Barents Sea.  
578 *Quaternary Science Reviews* **92**, 208–226 (2014). URL [http://www.sciencedirect.com/  
579 science/article/pii/S027737911300348X](http://www.sciencedirect.com/science/article/pii/S027737911300348X).
- 580 [86] Bjarnadóttir, L. R., Winsborrow, M. C. M. & Andreassen, K. Large subglacial meltwater features  
581 in the central Barents Sea. *Geology* **45**, 159 (2017). URL [http://dx.doi.org/10.1130/  
582 G38195.1](http://dx.doi.org/10.1130/G38195.1).
- 583 [87] Newton, A. M. W. & Huuse, M. Glacial geomorphology of the central Barents Sea: Implications for  
584 the dynamic deglaciation of the Barents Sea Ice Sheet. *Marine Geology* **387**, 114–131 (2017). URL  
585 <http://www.sciencedirect.com/science/article/pii/S0025322716302614>.
- 586 [88] Andreassen, K., Laberg, J. S. & Vorren, T. O. Seafloor geomorphology of the SW Barents Sea  
587 and its glaci-dynamic implications. *Geomorphology* **97**, 157–177 (2008). URL [http://www.  
588 sciencedirect.com/science/article/pii/S0169555X07002917](http://www.sciencedirect.com/science/article/pii/S0169555X07002917).
- 589 [89] Andreassen, K., Bjarnadóttir, L. R., Rüther, D. C. & Winsborrow, M. C. M. Retreat patterns and  
590 dynamics of the former Bear Island Trough Ice Stream. *Geological Society, London, Memoirs* **46**,  
591 445–452 (2016). URL <http://mem.lyellcollection.org/content/46/1/445>.
- 592 [90] Bartels, M. *et al.* Atlantic Water advection vs. glacier dynamics in northern Spitsbergen since early  
593 deglaciation. *Climate of the Past* **13**, 1717–1749 (2017). URL [https://www.clim-past.  
594 net/13/1717/2017/](https://www.clim-past.net/13/1717/2017/).
- 595 [91] Bjarnadóttir, L. R. & Andreassen, K. Ice-stream landform assemblage in Kveithola, western Barents  
596 Sea margin. *Geological Society, London, Memoirs* **46**, 325–328 (2016). URL [http://mem.  
597 lyellcollection.org/content/46/1/325](http://mem.lyellcollection.org/content/46/1/325).
- 598 [92] Bjarnadóttir, L. R., Rüther, D. C., Winsborrow, M. C. M. & Andreassen, K. Grounding-line dynamics  
599 during the last deglaciation of Kveithola, W Barents Sea, as revealed by seabed geomorphology  
600 and shallow seismic stratigraphy. *Boreas* **42**, 84–107 (2013). URL [http://dx.doi.org/10.  
601 1111/j.1502-3885.2012.00273.x](http://dx.doi.org/10.1111/j.1502-3885.2012.00273.x).
- 602 [93] Bondevik, S., Mangerud, J., Ronnert, L. & Salvigsen, O. Postglacial sea-level history of Edgeøya  
603 and Barentsøya, eastern Svalbard. *Polar Research* **14**, 153–180 (1995).
- 604 [94] Cadman, V. M. *Glacimarine sedimentation and environments during Late Weichselian and Holocene*  
605 *in the Bellsund Trough and Van Keulenfjorden, Svalbard*. Ph.D. thesis, University of Cambridge  
606 (1996).
- 607 [95] Esteves, M., Bjarnadóttir, L. R., Winsborrow, M. C. M., Shackleton, C. S. & Andreassen, K. Retreat  
608 patterns and dynamics of the Sentralbankrenna glacial system, central Barents Sea. *Quaternary*  
609 *Science Reviews* **169**, 131–147 (2017). URL [http://www.sciencedirect.com/science/  
610 article/pii/S0277379117300550](http://www.sciencedirect.com/science/article/pii/S0277379117300550).
- 611 [96] Hald, M., Danielsen, T. K. & Lorentzen, S. Late Pleistocene-Holocene benthic foraminiferal  
612 distribution in the southwestern Barents Sea: Paleoenvironmental implications. *Boreas* **18**, 367–388  
613 (1989).
- 614 [97] Hald, M. *et al.* Late-glacial and Holocene paleoceanography and sedimentary environments in the St.  
615 Anna Trough, Eurasian Arctic Ocean margin. *Palaeogeography, Palaeoclimatology, Palaeoecology*  
616 **146**, 229–249 (1999).

- 617 [98] Hogan, K. A. *et al.* Submarine landforms and ice-sheet flow in the Kvitøya Trough, northwestern  
618 Barents Sea. *Quaternary Science Reviews* **29**, 3545–3562 (2010).
- 619 [99] Hogan, K. A. *et al.* Subglacial sediment pathways and deglacial chronology of the northern Bar-  
620 ents Sea Ice Sheet. *Boreas* **46**, 750–771 (2017). URL <http://dx.doi.org/10.1111/bor.12248>.  
621
- 622 [100] Jessen, S. P., Rasmussen, T. L., Nielsen, T. & Solheim, A. A new Late Weichselian and Holocene ma-  
623 rine chronology for the western Svalbard slope 30,000–0 cal years BP. *Quaternary Science Reviews*  
624 **29**, 1301–1312 (2010). URL [http://www.sciencedirect.com/science/article/  
625 pii/S0277379110000521](http://www.sciencedirect.com/science/article/pii/S0277379110000521).
- 626 [101] Junttila, J., Aagaard-Sørensen, S., Husum, K. & Hald, M. Late Glacial–Holocene clay minerals  
627 elucidating glacial history in the SW Barents Sea. *Marine Geology* **276**, 71–85 (2010).
- 628 [102] Knies, J., Kleiber, H.-P., Matthiessen, J., Müller, C. & Nowaczyk, N. Marine ice-rafted debris records  
629 constrain maximum extent of Saalian and Weichselian ice-sheets along the northern Eurasian margin.  
630 *Global and Planetary Change* **31**, 45–64 (2001).
- 631 [103] Kleiber, H. P., Knies, J. & Niessen, F. The Late Weichselian glaciation of the Franz Victoria Trough,  
632 northern Barents Sea: ice sheet extent and timing. *Marine Geology* **168**, 25–44 (2000).
- 633 [104] Kristensen, D. K., Rasmussen, T. L. & Koç, N. Palaeoceanographic changes in the northern Barents  
634 Sea during the last 16 000 years—new constraints on the last deglaciation of the Svalbard–Barents  
635 Sea Ice Sheet. *Boreas* **42**, 798–813 (2013).
- 636 [105] Landvik, J. Y. *et al.* The last glacial maximum of Svalbard and the Barents Sea area: ice sheet extent  
637 and configuration. *Quaternary Science Reviews* **17**, 43–75 (1998).
- 638 [106] Lantzsch, H. *et al.* Deglacial to Holocene history of ice-sheet retreat and bottom current strength  
639 on the western Barents Sea shelf. *Quaternary Science Reviews* **173**, 40–57 (2017). URL [http://  
640 www.sciencedirect.com/science/article/pii/S0277379117300525](http://www.sciencedirect.com/science/article/pii/S0277379117300525).
- 641 [107] Lubinski, D. J. *et al.* The last deglaciation of the Franz Victoria Trough, northern Barents Sea. *Boreas*  
642 **25**, 89–100 (1996).
- 643 [108] Lubinski, D. J., Polyak, L. & Forman, S. L. Freshwater and Atlantic water inflows to the deep  
644 northern Barents and Kara seas since ca 13 <sup>14</sup>C ka: foraminifera and stable isotopes. *Quaternary  
645 Science Reviews* **20**, 1851–1879 (2001).
- 646 [109] Lucchi, R. G. *et al.* Postglacial sedimentary processes on the Storfjorden and Kveithola trough  
647 mouth fans: Significance of extreme glacial marine sedimentation. *Global and Planetary Change* **111**,  
648 309–326 (2013). URL [http://www.sciencedirect.com/science/article/pii/  
649 S0921818113002270](http://www.sciencedirect.com/science/article/pii/S0921818113002270).
- 650 [110] Nielsen, T. & Rasmussen, T. L. Reconstruction of ice sheet retreat after the last glacial maximum in  
651 storfjorden, southern svalbard. *Marine Geology* **402**, 228–243 (2018).
- 652 [111] Ottesen, D., Dowdeswell, J. A. & Rise, L. Submarine landforms and the reconstruction of fast-  
653 flowing ice streams within a large Quaternary ice sheet: The 2500-km-long Norwegian-Svalbard  
654 margin (57°–80°N). *GSA Bulletin* **117**, 1033 (2005). URL [+http://dx.doi.org/10.1130/  
655 B25577.1](http://dx.doi.org/10.1130/B25577.1).
- 656 [112] Patton, H. *et al.* Geophysical constraints on the dynamics and retreat of the Barents Sea ice sheet as a  
657 paleobenchmark for models of marine ice sheet deglaciation. *Reviews of Geophysics* **53**, 1051–1098  
658 (2015). URL <http://dx.doi.org/10.1002/2015RG000495>.
- 659 [113] Pau, M. & Hammer, Ø. Sedimentary environments in the south-western Barents Sea during the last  
660 deglaciation and the Holocene: a case study outside the Ingøydjupet trough. *Polar Research* **35**,  
661 23104 (2016). URL <https://doi.org/10.3402/polar.v35.23104>.
- 662 [114] Piasecka, E. D., Winsborrow, M. C. M., Andreassen, K. & Stokes, C. R. Reconstructing the retreat  
663 dynamics of the Bjørnøyrenna Ice Stream based on new 3D seismic data from the central Barents  
664 Sea. *Quaternary Science Reviews* **151**, 212–227 (2016). URL [http://www.sciencedirect.  
665 com/science/article/pii/S027737911630347X](http://www.sciencedirect.com/science/article/pii/S027737911630347X).

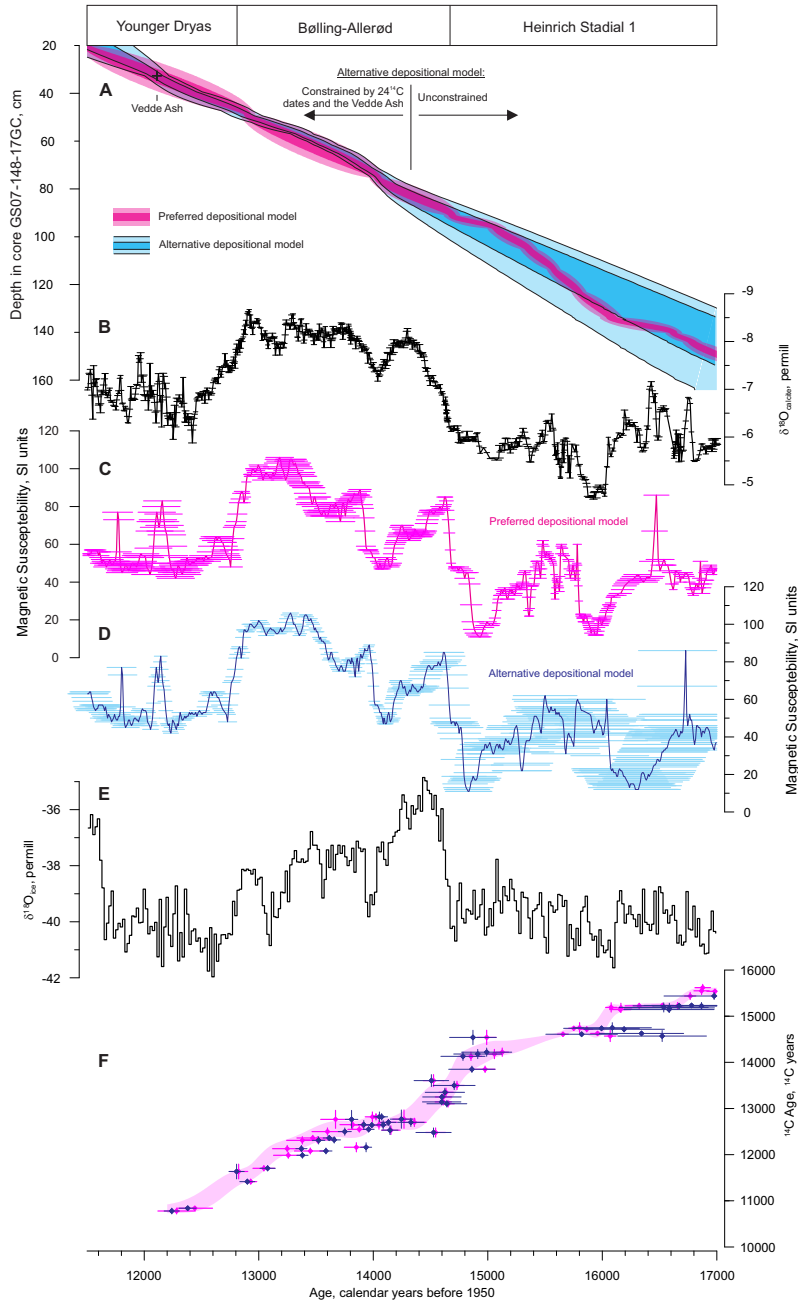
- 666 [115] Polyak, B., Lehman, S. J., Gataullin, V. & Jull, A. J. T. Two-step deglaciation of the southeastern  
667 Barents Sea. *Geology* **23**, 567–571 (1995).
- 668 [116] R  ther, D. C., Mattingsdal, R., Andreassen, K., Forwick, M. & Husum, K. Seismic architecture  
669 and sedimentology of a major grounding zone system deposited by the Bj  rn  yrenna Ice Stream  
670 during Late Weichselian deglaciation. *Quaternary Science Reviews* **30**, 2776–2792 (2011). URL <http://www.sciencedirect.com/science/article/pii/S0277379111001831>.  
671
- 672 [117] R  ther, D. C. *et al.* Pattern and timing of the northwestern Barents Sea Ice Sheet deglaciation and  
673 indications of episodic Holocene deposition. *Boreas* **41**, 494–512 (2012). URL <http://dx.doi.org/10.1111/j.1502-3885.2011.00244.x>.  
674
- 675 [118] R  ther, D. C., Winsborrow, M., Andreassen, K. & Forwick, M. Grounding line proximal sediment  
676 characteristics at a marine-based, late-stage ice stream margin. *Journal of Quaternary Science* **32**,  
677 463–474 (2017). URL <http://dx.doi.org/10.1002/jqs.2939>.
- 678 [119] Salvigsen, O. Radiocarbon dated raised beaches in Kong Karls Land, Svalbard, and their conse-  
679 quences for the glacial history of the Barents Sea area. *Geografiska Annaler: Series A, Physical*  
680 *Geography* **63**, 283–291 (1981).
- 681 [120]   lubowska-Woldengen, M. *et al.* Advection of Atlantic Water to the western and northern Svalbard  
682 shelf since 17,500 calyr BP. *Quaternary Science Reviews* **26**, 463–478 (2007).
- 683 [121] Svendsen, J. I., Elverh  y, A. & Mangerud, J. The retreat of the Barents Sea Ice Sheet on the west-  
684 ern Svalbard margin. *Boreas* **25**, 244–256 (1996). URL [http://dx.doi.org/10.1111/j.](http://dx.doi.org/10.1111/j.1502-3885.1996.tb00640.x)  
685 [1502-3885.1996.tb00640.x](http://dx.doi.org/10.1111/j.1502-3885.1996.tb00640.x).
- 686 [122] Winsborrow, M. C. M., Stokes, C. R. & Andreassen, K. Ice-stream flow switching during deglacia-  
687 tion of the southwestern Barents Sea. *GSA Bulletin* **124**, 275 (2012). URL [+http://dx.doi.org/10.1130/B30416.1](http://dx.doi.org/10.1130/B30416.1).  
688
- 689 [123] Amundsen, H. B. *et al.* Late Weichselian–Holocene evolution of the high-latitude And  ya submarine  
690 Canyon, north-Norwegian continental margin. *Marine Geology* **363**, 1–14 (2015).
- 691 [124] Bugge, T. *  vre lags geologi p   kontinentalsokkelen utenfor M  re og Tr  ndelag* (IKU, Institutt for  
692 Kontinentalsokkelunders  kelser, 1980).
- 693 [125] Holtedahl, H. & Bjerkli, K. Late Quaternary sediments and stratigraphy on the continental shelf off  
694 M  re-Tr  ndelag, W. Norway. *Marine Geology* **45**, 179205–202226 (1982).
- 695 [126] King, E. L., Haflidason, H., Sejrup, H. P. & L  vlie, R. Glacigenic debris flows on the North Sea  
696 Trough Mouth Fan during ice stream maxima. *Marine Geology* **152**, 217–246 (1998). URL <http://www.sciencedirect.com/science/article/pii/S0025322798000723>.  
697
- 698 [127] Laberg, J. S. *et al.* Late Quaternary palaeoenvironment and chronology in the Tr  nadjupet Slide area  
699 offshore Norway. *Marine Geology* **188**, 35–60 (2002). URL <http://www.sciencedirect.com/science/article/pii/S0025322702002748>.  
700
- 701 [128] Laberg, J. S., Eilertsen, R. S., Salomonsen, G. R. & Vorren, T. O. Submarine push moraine  
702 formation during the early Fennoscandian Ice Sheet deglaciation. *Quaternary Research* **67**,  
703 453–462 (2007). URL <http://www.sciencedirect.com/science/article/pii/S003358940700018X>.  
704
- 705 [129] Laberg, J. S., Eilertsen, R. S. & Salomonsen, G. R. Deglacial dynamics of the Vestfjorden –  
706 Tr  nadjupet palaeo-ice stream, northern Norway. *Boreas* **47**, 225–237 (2018). URL <http://dx.doi.org/10.1111/bor.12261>.  
707
- 708 [130] Nyg  rd, A., Sejrup, H. P., Haflidason, H., Cecchi, M. & Ottesen, D. Deglaciation history of the  
709 southwestern Fennoscandian Ice Sheet between 15 and 13 14C ka BP. *Boreas* **33**, 1–17 (2004).
- 710 [131] Nyg  rd, A. *et al.* Extreme sediment and ice discharge from marine-based ice streams: New evi-  
711 dence from the North Sea. *Geology* **35**, 395 (2007). URL [+http://dx.doi.org/10.1130/G23364A.1](http://dx.doi.org/10.1130/G23364A.1).  
712

- 713 [132] Rokoengen, K. & Bugge, T. Quaternary geology and deglaciation of the continental shelf off Troms,  
714 north Norway. *Boreas* **8**, 217–227 (1979).
- 715 [133] Rokoengen, K. & Frengstad, B. Radiocarbon and seismic evidence of ice-sheet extent and the  
716 last deglaciation on the mid-Norwegian continental shelf. *Norsk Geologisk Tidsskrift* **79**, 129–132  
717 (1999).
- 718 [134] Sejrup, H. P., Nygård, A., Hall, A. M. & Hafliðason, H. Middle and Late Weichselian (Devensian)  
719 glaciation history of south-western Norway, North Sea and eastern UK. *Quaternary Science Reviews*  
720 **28**, 370–380 (2009). URL [http://www.sciencedirect.com/science/article/pii/  
721 S0277379108002990](http://www.sciencedirect.com/science/article/pii/S0277379108002990).
- 722 [135] Vorren, T. O. & Kristoffersen, Y. Late Quaternary glaciation in the south-western Barents Sea.  
723 *Boreas* **15**, 51–59 (1986). URL [http://dx.doi.org/10.1111/j.1502-3885.1986.  
724 tb00742.x](http://dx.doi.org/10.1111/j.1502-3885.1986.tb00742.x).
- 725 [136] Vorren, T. O. & Plassen, L. Deglaciation and palaeoclimate of the Andfjord-Vågsfjord area, North  
726 Norway. *Boreas* **31**, 97–125 (2002). URL [http://dx.doi.org/10.1111/j.1502-3885.  
727 2002.tb01060.x](http://dx.doi.org/10.1111/j.1502-3885.2002.tb01060.x).
- 728 [137] Trauth, M. H. TURBO2: A MATLAB simulation to study the effects of bioturbation on paleoceanographic  
729 time series. *Computers & geosciences* **61**, 1–10 (2013).
- 730 [138] Sejrup, H. P., Clark, C. D. & Hjelstuen, B. O. Rapid ice sheet retreat triggered by ice stream debut-  
731 tressing: Evidence from the North Sea. *Geology* **44**, 355–358 (2016).
- 732 [139] Becker, L. W., Sejrup, H. P., Hjelstuen, B. O., Hafliðason, H. & Dokken, T. M. Ocean-ice sheet  
733 interaction along the se nordic seas margin from 35 to 15 ka bp. *Marine Geology* **402**, 99–117  
734 (2018).
- 735 [140] Newton, A. J., Dugmore, A. J. & Gittings, B. M. Tephabase: tephrochronology and the development  
736 of a centralised european database. *Journal of Quaternary Science* **22**, 737–743 (2007).

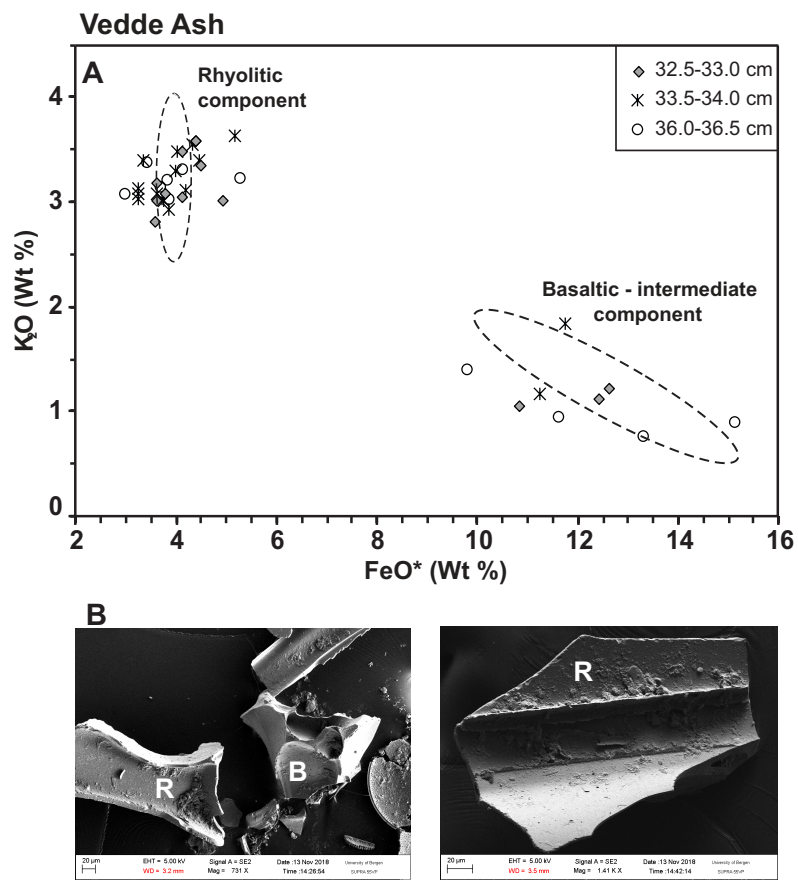
## Supplementary Figures



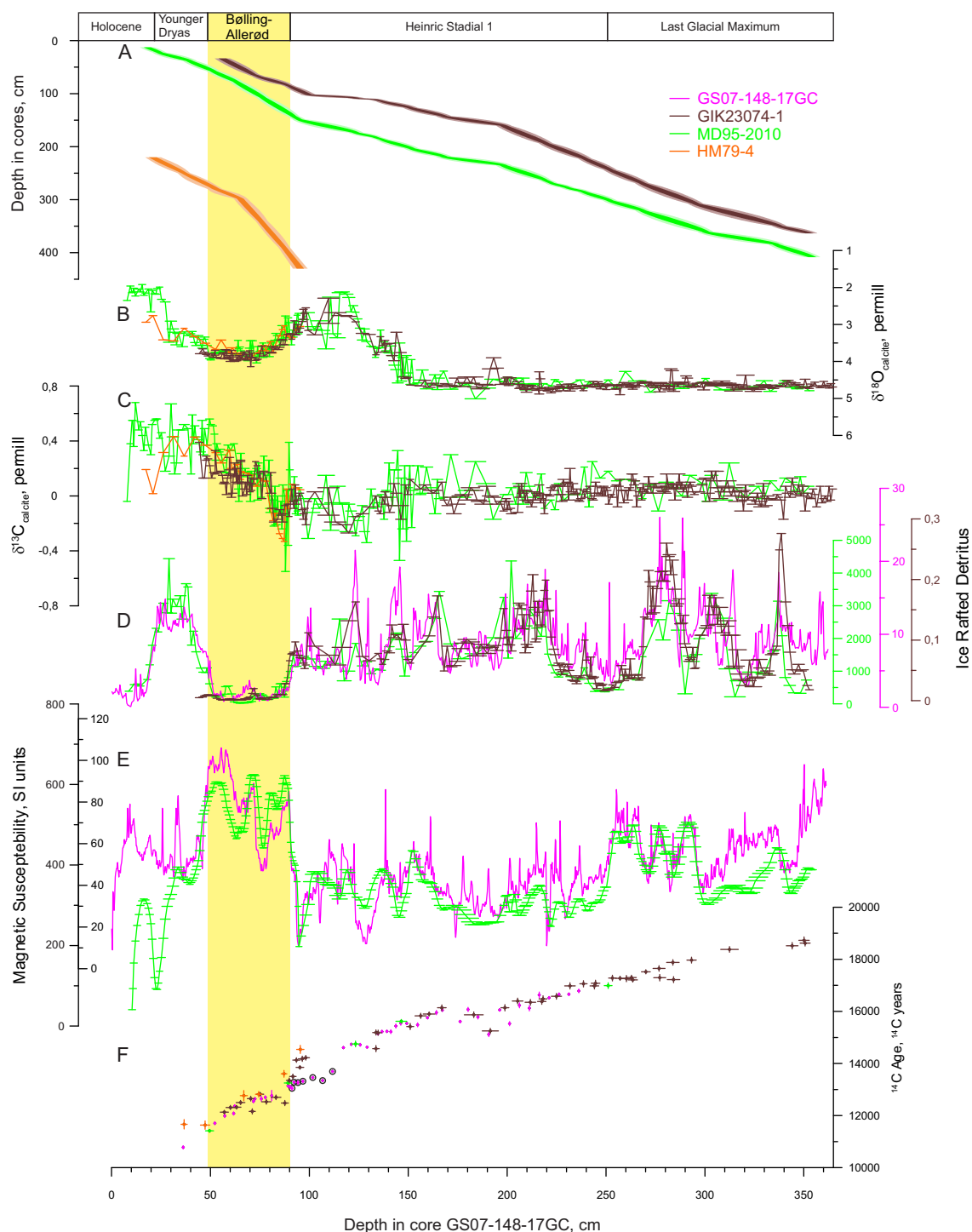
Supplementary Figure 1: Age-model of the Norwegian Sea core GS07-148-17GC. **A**, Age model constructed using the P\_Sequence option in OxCal<sup>63</sup>. The dark- and light-colored bands represent the respective 68.2% and 95.4% credible intervals of the model. The model is made by defining tie-points (diamonds and vertical dashes between **B**) and **(C)**) between the magnetic susceptibility record of core GS07-148-17GC (**C**) and the  $\delta^{18}\text{O}$  record from Hulu cave (**B**)<sup>27</sup>. While the Bølling transition is associated with high sedimentation rates and deposition of plumites closer to the continental shelf edge and the ice sheet grounding line<sup>82,100,109</sup>, core GS07-148-17GC is located in a more distal setting where the direct influence from sediment-laden meltwater plumes is less likely. The interval with high sedimentation rates centered at about 17.5 kyr cal BP is related to the deposition of a plumite sourced from the Norwegian Channel Ice Stream<sup>71-73,138,139</sup>. Horizontal error bars in **B-C** represent the  $1\sigma$  uncertainty of the Oxcal-generated age-model for the respective records. **(D)**, The average of the  $\delta^{18}\text{O}$  record from the Greenland summit ice cores (GISP2 and GRIP aligned on the GICC05 chronology<sup>30</sup>), which is plotted for reference. The peak occurrence of the Vedde Ash in core GS07-148-17GC and the Greenland ice cores is indicated by the blue line. Note that the Vedde Ash has not been used to constrain the GS07-148-17GC chronology, yet the difference in the Vedde Ash ages is only 10 years. **E**, The distribution of tephra shards found in core GS07-148-17GC, including rhyolitic (black) and basaltic (red) shards. Arrows mark levels sampled for geochemical analyses of tephra shards (Supplementary Fig. 3).



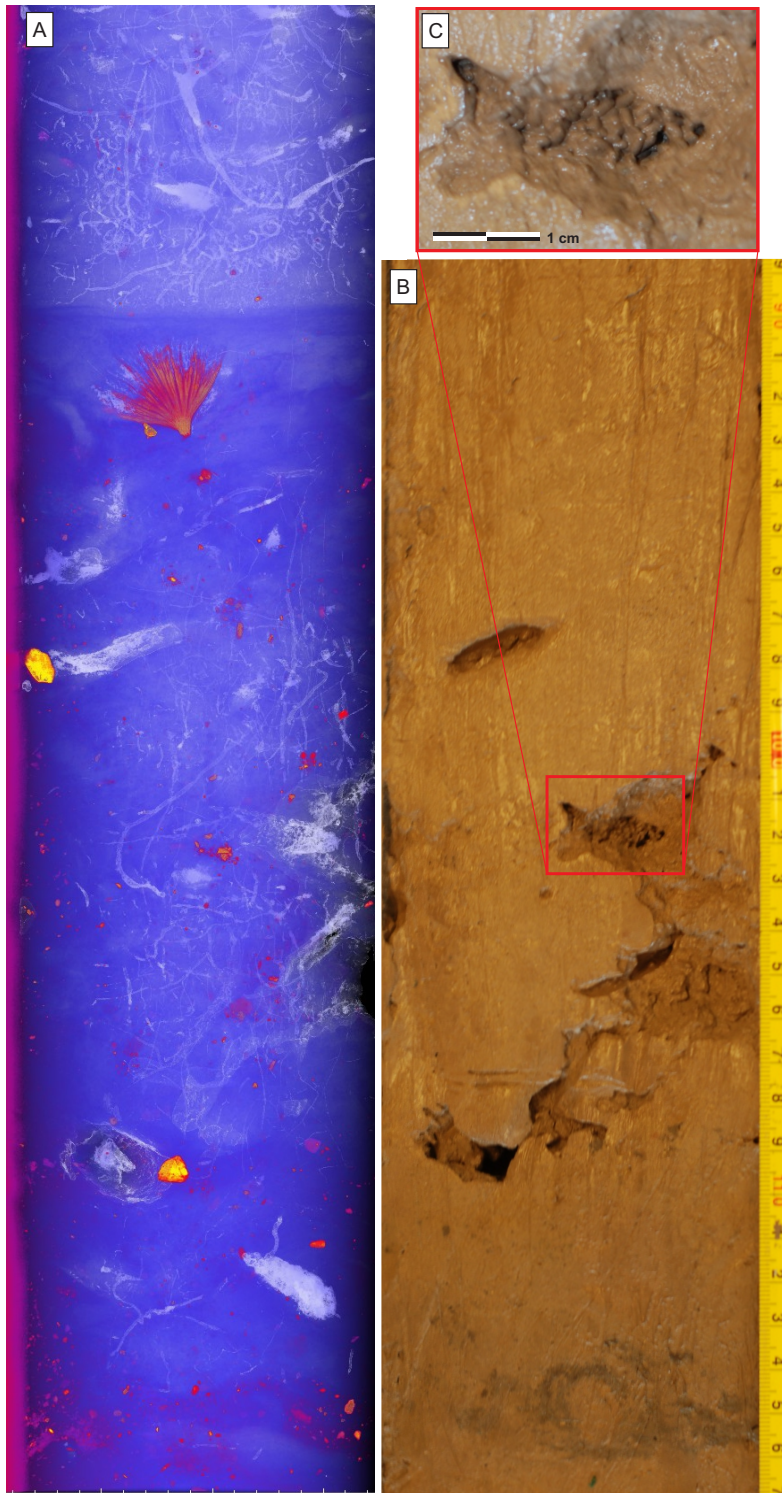
Supplementary Figure 2: Alternative depositional model of core GS07-148-17GC. **A**, comparison of the preferred deposition model (Magenta; Supplementary Fig. 1) and our alternative deposition model (cyan). Darker and lighter color represents the 68.2% and 95.4% credible intervals, respectively. The positions of the Vedde Ash, and the constrained and unconstrained segments of the models are indicated. **B**, The  $\delta^{18}\text{O}$  record from Hulu cave as in Supplementary Fig. 1<sup>27</sup>. **C-D**, the MS record of core GS07-148-17GC on the preferred (**C**, magenta) and alternative (**D**, blue) deposition model. The horizontal error bars in **B**, **C** and **D** represent the  $1\sigma$  uncertainty of the Oxcal-generated deposition models for the respective records. **E**, the average of the  $\delta^{18}\text{O}$  record from the Greenland summit ice cores (GISP2 and GRIP aligned on the GICC05 chronology<sup>30</sup>) plotted for reference. **F**, the  $^{14}\text{C}$  ages of the Norwegian Sea compilation plotted both on our preferred chronology (magenta) and the alternative chronology (blue), the light pink field is the Norwegian Sea  $^{14}\text{C}$  reconstruction.



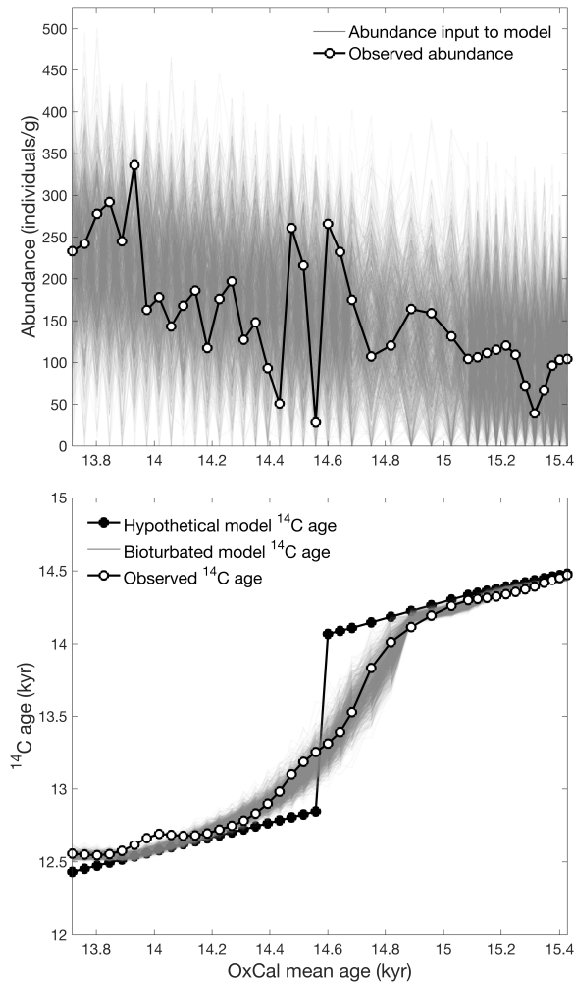
Supplementary Figure 3: The Vedde ash in core GS07-148-17GC. **A**, Bivariate plot of  $\text{FeO}^*$  vs  $\text{K}_2\text{O}$  showing the results from all the data presented in the Supplementary data File. All data are normalized to a 100% total on a water and volatile-free basis for data set comparison (the Supplementary Data File contains the original non-normalized geochemical data). Total iron is expressed as  $\text{FeO}^*$ . Compositional envelopes (dash lines) show the rhyolitic and basaltic-intermediate components of the Vedde Ash (from Tephabase: [www.tephabase.org](http://www.tephabase.org) <sup>140</sup>). **B**, Scanning electron microscope images of glass shards from interval 32.5-33.0 cm depth in core GS07-148-17GC (B: basaltic glass, R: rhyolitic glass).



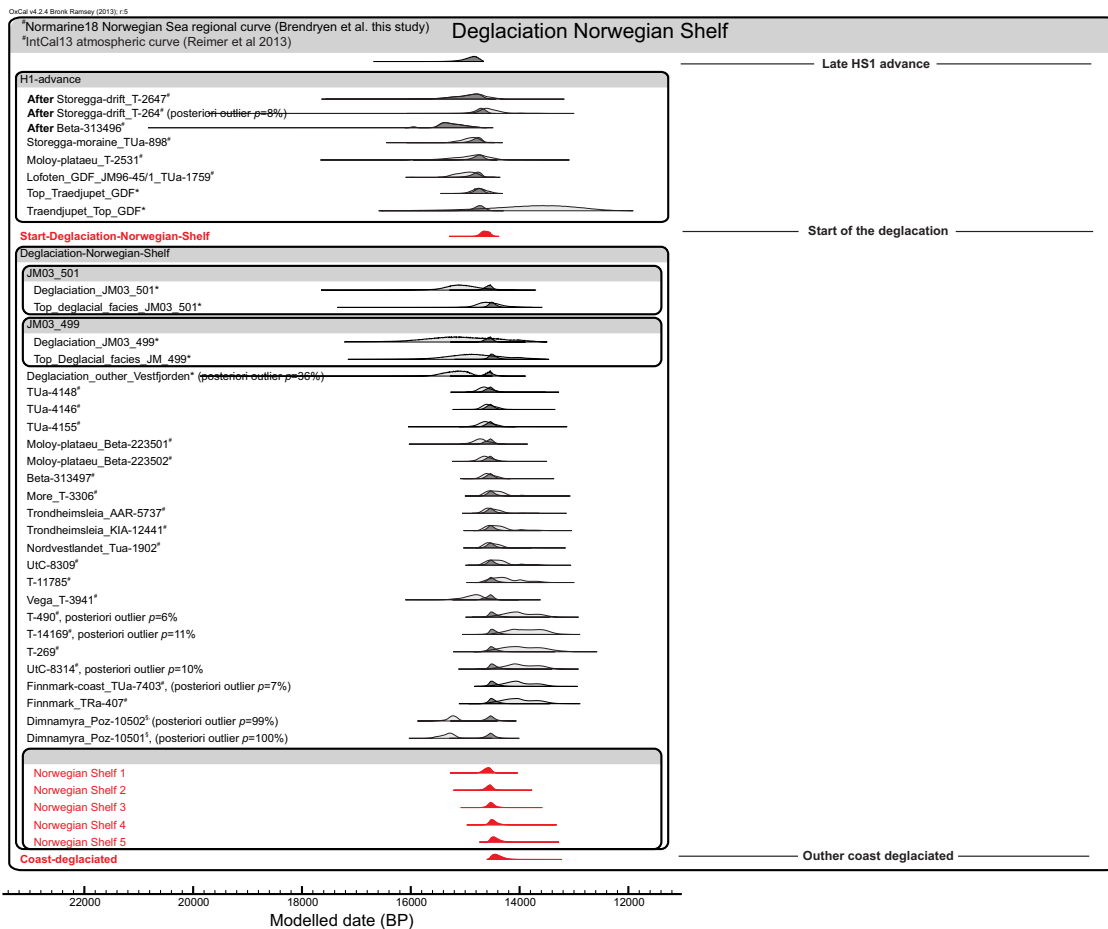
Supplementary Figure 4: Norwegian Sea data records plotted on GS07-148-17GC depth scale. **A**, Depth models of cores HM79-4, GIK23074-1 and MD95-2010 constructed using the P\_Sequence option in OxCal<sup>63</sup>. Light-colored uncertainty envelopes represent the 95.4% quantiles, while darker colored represent the 68.2% quantiles of the depth model PDF. The models are made by defining tie-point between the cores and core GS07-148-17GC using the records of **(B)**  $\delta^{18}\text{O}^{31-33}$ , **(C)**  $\delta^{13}\text{C}^{31-33}$ , **(D)** IRD<sup>31,33</sup>, and **(E)** magnetic susceptibility<sup>33</sup>. **F**, Compiled AMS  $^{14}\text{C}$ <sup>31-34</sup>. Circles mark the dates that are excluded from further analysis due to distortion of the core stratigraphy from deep burrows (Supplementary Fig. 5). Horizontal error bars in **B-F** represent the  $1\sigma$  uncertainty of the depth model for the respective cores.



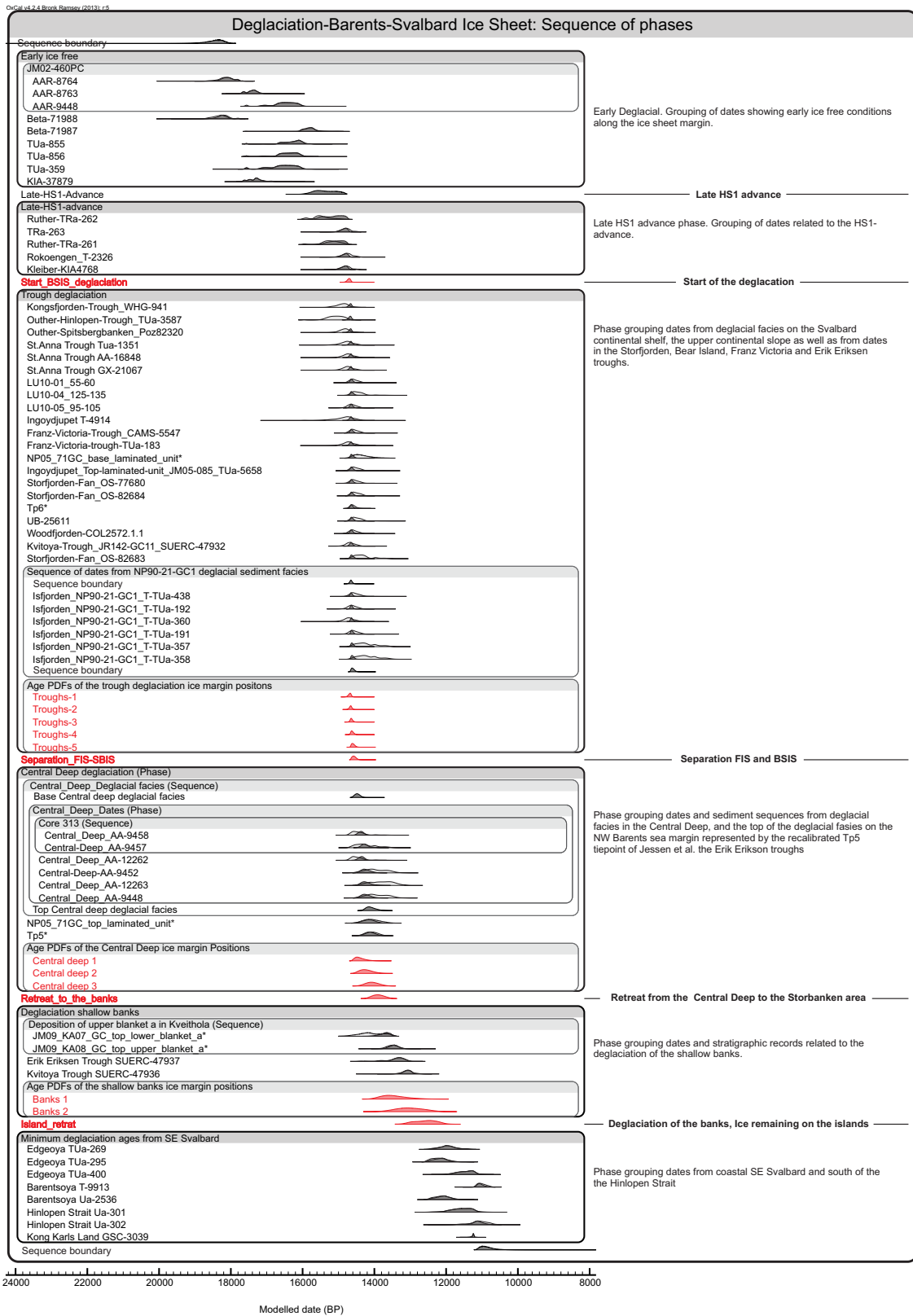
Supplementary Figure 5: Trace fossils and burrows between 83 and 117 cm depth in core GS07-148-17GC. **A**, Computed tomography radiograph with colour scheme chosen to emphasise trace fossils and burrows. White and light blue colours indicate low-density sediments and cavities, red and yellow colours mark high-density material. **B**, Photograph of the core surface showing open burrow tubes and cavities. **C**, Close-up of burrow cavity with ovoid pellets.



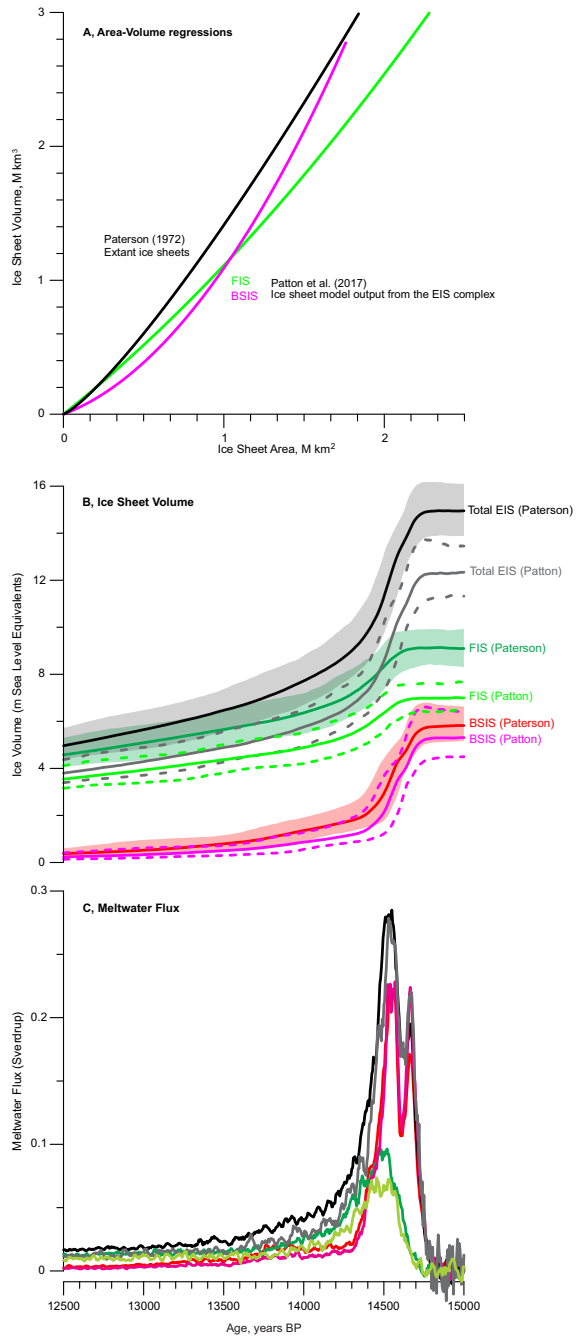
Supplementary Figure 6: The effect of bioturbation on the  $^{14}\text{C}$  reconstruction at the Bølling transition. To assess the potential impact of bioturbation, we used the TURBO2 model<sup>137</sup> (Methods). As input we used 1,024 simulated abundance vectors (gray; top panel) generated as normally distributed random values centered on the best-fit linear trend and with the standard deviation of the observed abundance of foraminifera in core MD95-2210<sup>33</sup> (top panel). If we assume a constant mixed layer depth of 6 cm, then the observed change in  $^{14}\text{C}$  age can be reproduced with reasonable accuracy in TURBO2 by invoking a hypothetical true  $^{14}\text{C}$  age with an abrupt step change 14.56 kyr ago (lower panel). This result is not an attempt to infer the true  $^{14}\text{C}$  age history, but rather to demonstrate that the effect of bioturbation would be to smear out the true event. As a consequence, our reconstruction is likely to overestimate the time scale of the EIS collapse and underestimate its contribution to the global MWP-1a.



Supplementary Figure 7: Bayesian deglacial chronology of the Norwegian continental shelf. As prior information, all radiocarbon dates or probability density functions of sediment unit boundaries are grouped into phases according to geographical and/or stratigraphical context. A phase in this context refers to a retreat (or advance) of the ice sheet in a specific area. The phases are ordered in a sequence following the relative chronological order. The PDF's of unmodeled conventional  $^{14}\text{C}$  dates are calibrated using the new Norwegian Sea  $^{14}\text{C}$  age reconstruction (Fig. 2) and is shown as light gray. Dark gray mark the modeled posteriori PDF of the same dates. Red PDF's show the posteriori age probabilities of undated events that corresponds to reconstructed ice margins depicted in Fig. (1).



Supplementary Figure 8: Bayesian deglacial chronology of the Barents-Svalbard ice sheet. As prior information, all radiocarbon dates or probability density functions of sediment unit boundaries are grouped into phases according to geographical and/or stratigraphical context. A phase in this context refers to a retreat (or advance) of the ice sheet in a specific area. The phases are ordered in a sequence following the relative chronological order. The PDF's of unmodeled conventional  $^{14}\text{C}$  dates are calibrated using the new Norwegian Sea  $^{14}\text{C}$  age reconstruction (Fig. 2) and is shown as light gray. Dark gray mark the modeled posteriori PDF of the same dates. Red PDF's show the posteriori age probabilities of undated events that corresponds to reconstructed ice margins depicted in Fig. (1).



Supplementary Figure 9: Comparison between area-volume regressions. **A**, Regression lines of ice sheet area and volume data used to convert the EIS area reconstruction to volume with the regression of<sup>37</sup> through six extant ice sheets (black) and regression lines (2nd order polynomial fits) through the EIS modeling output from<sup>38</sup> (green and purple). FIS, Fennoscandian Ice Sheet; BSIS, Barents Svalbard Ice Sheet; BHS, British Isles Ice Sheet. **B**, Comparison of the EIS volume estimated by the regression of<sup>37</sup> and a 2nd order polynomial regression of ice sheet specific area-volume output from a transient model simulation of the growth and decay of the EIS complex of<sup>38</sup>. **C**, The corresponding meltwater fluxes. Color codes are the same as in **B**.